
Bayesian Rain Field Reconstruction using Commercial Microwave Links and Diffusion Model Priors

Badr Moufad^{*1} Albina Ilina^{*2} Hai Victor Habi³ Salem Lahlou² Yazid Janati⁴ Hagit Messer³
Eric Moulines^{2,5}

Abstract

Commercial Microwave Links (CMLs) offer dense spatial coverage for rainfall sensing but produce path-integrated measurements that make accurate ground-level reconstruction challenging. Existing methods typically oversimplify CMLs as point sensors and neglect line integration relating rainfall to signal attenuation, resulting in degraded performance under heterogeneous precipitation. In this work, we view rain field reconstruction as a Bayesian inverse problem with Diffusion Models (DMs) as high-fidelity spatial priors. We show that diffusion models better preserve key rainfall statistics compared to censored Gaussian processes. Framing rainfall estimation as a Bayesian inverse problem with a DM prior enables training-free posterior sampling using a broad family of methods, including Plug-and-Play, Sequential Monte Carlo, and Replica Exchange methods. Experiments on synthetic and real-world datasets demonstrate consistent improvements over established CML-based reconstruction baselines.

1. Introduction

Accurate rain fields are central to hydrology, flood warning, and water resource management. Standard sensing relies on Rain Gauges (RGs), weather radars, and satellites. RGs are accurate but sparse (Messer et al., 2022). Weather radars provide broad coverage, yet require calibration and are sensitive to clutter and atmospheric effects (Michelson & Koistinen, 2000; Krajewski & Smith, 2002;

Harrison et al., 2000). Weather satellites extend coverage to data-scarce regions but often trade resolution for reach (Funk et al., 2014). Hence, no single modality provides dense, accurate, and affordable precipitation monitoring at scale. Opportunistic remote sensing addresses this gap by reusing existing infrastructure. In particular, *Commercial Microwave Links* (CMLs) in cellular backhaul networks can act as near-ground rain sensors (Messer et al., 2006; Uijlenhoet et al., 2018; Graf et al., 2020; 2026). CMLs form dense networks of transmitters and receivers deployed for telecommunication purposes. During precipitation, rainfall induces attenuation along each link path $\{\mathcal{L}_i\}_{i=1}^m$ of the network, which is commonly modeled by the empirical power law (Leijnse et al., 2007; Eshel et al., 2021)

$$Y_i = a \int_{\mathbf{s} \in \mathcal{L}_i} X(\mathbf{s})^b d\mathcal{L}_i + \sigma_i Z_i, \quad Z_i \sim \mathcal{N}(0, 1), \quad (1)$$

where $X(\mathbf{s})$ is the rain rate (mm/h), and (a, b) are constants that depend on the characteristics of the link, while $\sigma_i Z_i$ is an additive Gaussian noise of standard deviation σ_i independent of the attenuation Y_i .

Rain-field reconstruction from CMLs is an inverse problem: for a region of interest $\Omega \subset \mathbb{R}^2$, and given attenuations $\{Y_i\}_{i=1}^m$, estimate the gridded field in an $H \times W$ domain. The problem is ill-posed because measurements are path-integrated and nonlinear. Many reconstruction methods approximate each link as a *Virtual Rain Gauge* (VRG) and then interpolate (Shepard, 1968; Vereem et al., 2013; Goldshtein et al., 2009; Eshel et al., 2021), which can discard valuable spatial information and degrade under heterogeneous rainfall. More elaborate variants, e.g., multiple VRGs per link, still inherit interpolation limitations (Goldshtein et al., 2009). The fundamental challenge is that CML measurements provide aggregate information along paths, whereas reconstruction requires resolving fine-scale spatial structure. This mismatch is a hallmark of ill-posed inverse problems: infinitely many rain fields can produce identical observations. Regularization through prior knowledge is essential, yet classical choices such as isotropic smoothness or Gaussian spatial models fail to capture the complex, multi-scale, and intermittent structure of real precipitation. In this work, we instead cast CML-based rain

^{*}Equal contribution ¹CMAF, Ecole Polytechnique, France ²MBZUAI, UAE ³School of Electrical and Computer Engineering, Tel Aviv University, Tel Aviv, Israel ⁴IFM, France ⁵EPITA, France. Correspondence to: Badr Moufad <badr.moufad@polytechnique.edu>, Hai Victor Habi <haivictorh@mail.tau.ac.il>.

field reconstruction as Bayesian inference with a learned generative prior. Recent works show that deep generative models, especially *Diffusion Models* (DMs), provide strong priors for inverse problems and are amenable to *training-free* posterior sampling via inference-time guidance (Daras et al., 2024; Janati et al., 2025b; Chung et al., 2023). This setting consists in training a DM offline on representative data and then reusing it at inference as a prior to regularize ill-posed inverse problems.

Building on this paradigm, we make the following contributions. **1** We show that DM priors yield high-fidelity spatial rain fields and improve key statistics, e.g. cumulative precipitation, compared to censored Gaussian Processes. **2** We leverage training-free posterior sampling to enable flexible inference with a fixed pre-trained DM, covering Plug-and-Play, Sequential Monte Carlo, and Replica Exchange approaches. **3** We move beyond VRG approximations by explicitly modeling the nonlinear, path-integrated CML operator governed by the empirical the power-law.

We validate the approach on simulated and real datasets, and observe consistent gains over established baselines. To the best of our knowledge, this is the first work to bring posterior sampling with diffusion priors to opportunistic rain sensing with CMLs. We also release our code¹.

2. Related Work

CMLs were originally proposed as opportunistic rainfall sensors based on the physically grounded relationship between rain-induced signal attenuation and path-integrated rainfall intensity (Messer et al., 2006). A dominant modeling assumption in much of the CML literature is to reduce each path-integrated CML measurement to a single point observation, typically assigned to the link midpoint, thereby ignoring rainfall variability along the link path. Under this abstraction, rainfall fields are reconstructed using deterministic point-based spatial interpolation methods such as Inverse Distance Weighting (IDW) and Ordinary Kriging (OK) (Zhang et al., 2023; Blettner et al., 2022; Messer et al., 2022). IDW estimates values at grid locations as weighted averages of nearby measurements, with weights decaying as a power of the distance, whereas OK exploits second-order spatial statistics and derives interpolation weights from the spatial correlation structure of the observed data through a variogram model. While these approaches are simple and computationally efficient, collapsing line-integral measurements into point estimates inherently discards rainfall variability information contained in the line-integral nature of CML measurements along the link path. As a consequence, the reconstructed fields are often overly smooth and fail to reproduce fine-scale spatial variability and localized

extremes. To mitigate this limitation, Messer et al. (2022); Eshel et al. (2021) proposed Goldshtein-Messer-Zinevich (GMZ) algorithm where multiple VRGs are used to approximate the path-integrated measurement. The VRGs are placed along the link, and their intensities are iteratively adjusted to ensure consistency with the original CML observation. While GMZ better represents sub-link variability, it ultimately remains within the interpolation framework, as it relies on pseudo-point measurements rather than directly assimilating the path-integral observations.

More advanced stochastic reconstruction methods (Haese et al., 2017; Hörning et al., 2019; Blettner et al., 2022), such as Random Mixing (RM), account for the path-integrated nature of CML measurements and, unlike interpolation methods, provide a principled treatment of reconstruction uncertainty. It generates precipitation fields as stochastic linear combinations of unconditional random fields that reproduce the observed spatial dependence structure. RG measurements are imposed as pointwise constraints, while CML observations enter as nonlinear, path-integrated constraints. Repeating this procedure over several steps yields an ensemble of spatial fields, allowing reconstruction uncertainty to be quantified. However, RM relies on the generation and optimization of large ensembles of unconditional random fields, which is computationally expensive, especially for country-scale applications. Besides, it is constrained by the need to specify marginal rainfall distributions and spatial dependence structures. This makes them rain-gauge dependent, as the reliable estimation of these statistical properties typically requires a sufficiently dense and gauge network for the marginals. Consequently, such methods are not well suited for use cases in which only a very limited number of rain gauges are available, or where rainfall information is derived almost exclusively from CMLs.

In this work, we focus on rain field reconstruction using only CML measurements. We provide an extended discussion of deterministic and stochastic CML-based reconstruction methods, including the Random Mixing framework and multi-sensor fusion approaches, in Section A.

3. Rain Field Prior Models

The choice of prior is critical for regularizing the ill-posed CML inverse problem. We compare two modeling approaches: (i) a censored Gaussian process that explicitly encodes rainfall characteristics such as spatial correlation and non-negativity, and (ii) DM that learns them directly from data.

3.1. Censored Gaussian Processes

Rainfall intensity fields are inherently intermittent: they combine frequent zero-precipitation events with highly

¹Link: github.com/Badr-MOUFAD/rainfield-diffusion-models

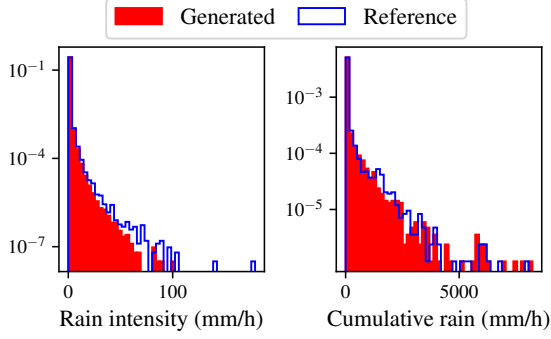


Figure 1. Comparison of rain field statistics between the reference samples and generated samples using the DM prior. The histograms show densities and are built using 5000 samples.

skewed positive intensities, as illustrated in Figure 1. There exists a rich literature on stochastic precipitation modeling and geostatistical reconstruction (Wilks & Wilby, 1999; Wheeler et al., 2000; Yang et al., 2005). A classical and widely used statistical abstraction models this mixed behavior through a latent Gaussian Process that is left censored at zero (Bardossy & Plate, 1992). Early frameworks (Bardossy & Plate, 1992; Ailliot et al., 2009) represent spatial dependence by a latent Gaussian random field and enforce non-negativity by censoring, often together with power-type transformations to better match the heavy right tail of positive rain rates. Subsequent work refined these ideas by introducing more complex transformations of the censored latent process in order to increase flexibility while retaining analytic and computational convenience (Baxeveni & Lennartsson, 2015; Stauffer et al., 2017). Despite their practical appeal, censored Gaussian Process (GP) priors remain limited by the structure of Gaussian kernels. In particular, Gaussian-based kernels tend to induce comparatively *stiff* priors: they can struggle to reproduce the sharp gradients, multi-scale variability, and nonstationary spatial organization that commonly arise in rain fields. In addition, when these models are used as priors within Bayesian inverse problems, inference can become computationally demanding. The censoring operation introduces inequality constraints and requires manipulating high-dimensional truncated or censored Gaussian distributions, which in turn involves prohibitive sampling procedures (Pakman & Paninski, 2014; Botev, 2017).

We adopt the following censored GP model as a classical baseline prior. The rain field X is defined on a $H \times W$ grid and is constructed from a latent Gaussian random field V . Specifically, we assume $V \sim \mathcal{GP}(\mu, k)$ with $\mu : \mathbb{R}^2 \rightarrow \mathbb{R}$. To accommodate anisotropy, we use a stationary kernel parameterized by a positive definite matrix $\mathbf{Q} \in \mathbb{R}^{2 \times 2}$:

$$k(\mathbf{s}, \mathbf{s}') = \sigma^2 \exp\left(-\frac{1}{2}(\mathbf{s} - \mathbf{s}')^\top \mathbf{Q} (\mathbf{s} - \mathbf{s}')\right),$$

where $\mathbf{s}, \mathbf{s}' \in \mathbb{R}^2$. The observed rain field is then obtained via a power transformation followed by censoring at zero,

$$X(\mathbf{s}) = \max(0, V(\mathbf{s})^\beta), \quad \text{for } \mathbf{s} \in \mathbb{R}^2,$$

which induces a point mass at zero together with a skewed positive component. The parameter β controls the degree of skewness in the positive intensities, while \mathbf{Q} and σ govern the spatial correlation structure and marginal scale, respectively. This model is parameterized by $(\mu, \mathbf{Q}, \sigma, \beta)$. The Expectation–Maximization algorithm (Ordoñez et al., 2018) is used to estimate the parameters of the model $(\mu, \mathbf{Q}, \sigma, \beta)$ which treats the latent field V as missing data and accounts for the censoring mechanism during inference; details are provided in Section F.

3.2. Diffusion Models

Let $x_0 \sim p_0$ denote a sample from the data distribution. We adopt the *Variance Exploding* (VE) formulation of Diffusion Models defined by fixing an increasing noise schedule $0 = \sigma_0 < \sigma_1 < \dots < \sigma_T$ (Song et al., 2021b; Karras et al., 2022). The corruption process is defined as a Markov chain that gradually perturbs the data via Gaussian noise,

$$q_{t+1|t}(x_{t+1} | x_t) = \mathcal{N}(x_t, (\sigma_{t+1}^2 - \sigma_t^2)\mathbf{I}), \quad (2)$$

for $t \in \llbracket 0, T-1 \rrbracket$. This construction yields the closed-form marginal $q_{t|0}(x_t | x_0) = \mathcal{N}(x_t; x_0, \sigma_t^2\mathbf{I})$, or equivalently $x_t = x_0 + \sigma_t \varepsilon$ with $\varepsilon \sim \mathcal{N}(0, \mathbf{I})$. The resulting joint distribution over the diffusion path factorizes as

$$p_{0:T}(x_{0:T}) = p_0(x_0) \prod_{t=0}^{T-1} q_{t+1|t}(x_{t+1} | x_t).$$

The same joint distribution also admits a backward factorization (Cappé et al., 2005)

$$p_{0:T}(x_{0:T}) = \left[\prod_{t=0}^{T-1} p_{t|t+1}(x_t | x_{t+1}) \right] p_T(x_T),$$

where, for sufficiently large σ_T , the terminal distribution p_T is well approximated by $\mathcal{N}(0, \sigma_T^2\mathbf{I})$. The reverse transition kernels $p_{t|t+1}$ are generally intractable, as they depend on the denoising posterior $p_{0|t}(x_0 | x_t) \propto p_0(x_0) q_{t|0}(x_t | x_0)$. Indeed, $p_{t|t+1}$ can be expressed using the latter as

$$p_{t|t+1}(x_t | x_{t+1}) = \mathbb{E}_{x_0 \sim p_{0|t}(\cdot | x_{t+1})} [q_{t|0,t+1}(x_t | x_0, x_{t+1})],$$

where the conditional transition $q_{\ell|0,t}$ for $0 < \ell < t$ admits a closed-form expression (Ho et al., 2020; Song et al., 2021a). In the VE setting, it is Gaussian with mean given by a convex combination of (x_0, x_t) ,

$$q_{\ell|0,t}(x_\ell | x_0, x_t) = \mathcal{N}\left(\gamma_{\ell|t} x_t + (1 - \gamma_{\ell|t}) x_0, \sigma_\ell^2 (1 - \gamma_{\ell|t}) \mathbf{I}\right),$$

where $\gamma_{\ell|t} = \sigma_\ell^2 / \sigma_t^2$. The commonly adopted surrogate for the intractable reverse kernel $p_{t|t+1}$ replaces the unknown

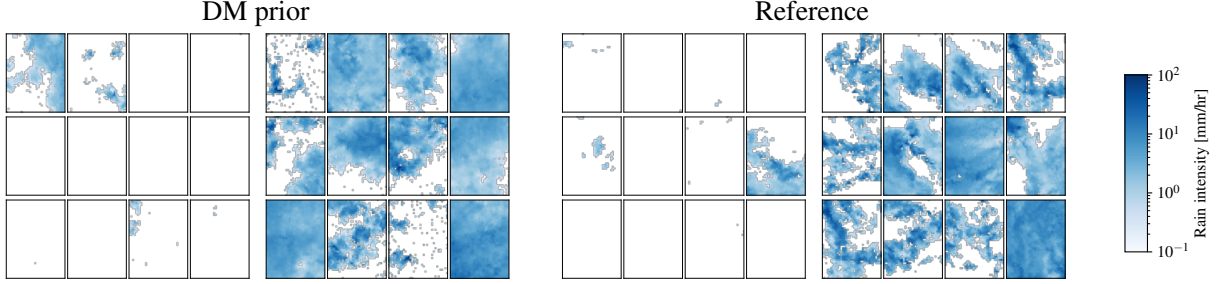


Figure 2. Examples of generated rain fields using the prior DM compared with reference rain fields. A total of 5,000 samples were generated. In each subfigure, on the left, samples are randomly drawn from the datasets; on the right, they are drawn from the top 90% wet samples by cumulative rain.

clean sample x_0 in the above transition with the output of a neural network $(t, x_t) \mapsto D_t^\theta(x_t)$ parameterized by θ . This yields the approximate reverse process

$$p_{t|t+1}^\theta(x_t | x_{t+1}) = q_{t|0,t+1}(x_t | D_{t+1}^\theta(x_{t+1}), x_{t+1}).$$

The neural network is trained to predict the posterior mean $D_t(x_t) := \int x_0 p_{0|t}(x_0|x_t)dx_0$ by minimizing a denoising regression objectives (Ho et al., 2020; Nichol & Dhariwal, 2021; Karras et al., 2022). After training, new samples are generated by initializing $x_T \sim \mathcal{N}(0, \sigma_T^2 \mathbf{I})$ and iteratively drawing samples from $p_{t|t+1}^\theta(\cdot|x_{t+1})$ down to x_0 .

3.3. Diffusion Model Prior on OpenMRG Data

We train a DM using the EDM framework (Karras et al., 2022) on the OpenMRG dataset (Andersson et al., 2022), which provides synchronized CML, radar, and RG measurements over Gothenburg during June–August 2015; refer to Section 5.2 for details. Training is performed on 21,196 radar-derived rain-rate fields, preprocessed with `PYNNcml` (Habi, 2026) and discretized on a 48×36 spatial grid. Additional implementation details are provided in Appendix B.

Evaluation of rain field priors. We evaluate the quality of the learned DM prior independently of the inverse problem, focusing on its ability to generate realistic rain fields. Figure 2 presents qualitative samples drawn from the DM alongside reference rain fields, while Figure 1 reports histograms of rain rates and cumulative precipitation. Both statistics show close agreement with the reference data, and the qualitative examples indicate that the trained DM preserves the sparse structure characteristic of rainfall fields.

To further assess distributional fidelity, we use a classifier two-sample test (Lopez-Paz & Oquab, 2016). Specifically, it consists of training a classifier to distinguish between a held-out set of real rain fields from generated samples by the diffusion prior. Classification accuracy close to 50% indicates that generated samples are difficult to distinguish

from real data, and therefore that the learned prior captures the target distribution well. We use the discriminator architecture of Habi & Messer (2021) and report classification accuracy on a balanced held-out test set as the evaluation metric. The trained discriminator achieves 57% accuracy, where chance level is 50%, indicating only limited distinguishability between generated and real rainfall fields. We provide more implementation details in Section B.

4. Posterior Sampling with Diffusion Models

We now formulate CML-based rainfall reconstruction as a Bayesian inverse problem and describe training-free posterior sampling methods that leverage pre-trained DM prior.

CML Measurement Operator. Let $X : \Omega \rightarrow \mathbb{R}_+$ be a rain field and let $x_0 \in \mathbb{R}_+^{H \times W}$ denote its discretization on grid points $\{s_k\}_{k=1}^{HW}$, with entries $[x_0]_k = X(s_k)$. The measurement of the CML at the i -link \mathcal{L}_i is described by a power-law parameters (a, b) , and a noise level σ_i as

$$Y_i = a \int_{s \in \mathcal{L}_i} X(s)^b d\mathcal{L}_i + \sigma_i Z_i, \quad Z_i \sim \mathcal{N}(0, 1). \quad (3)$$

Under the standard piecewise-constant assumption on grid cells (Eshel et al., 2021), the line integral can be approximated by a weighted sum

$$Y_i = a \sum_{k=1}^{HW} \Delta_k^i [x_0]_k^b + \sigma_i Z_i = \langle a \Delta^i, x_0^b \rangle + \sigma_i Z_i, \quad (4)$$

where *abuse the notation* and use x_0^b to denote the element-wise b -th power, Δ_k^i is the intersection length between the link path \mathcal{L}_i and cell k , and $\langle \cdot, \cdot \rangle$ is the Frobenius inner product. Stacking the m links gives the observation model $y = \mathcal{M}(x_0) + \Sigma z$ with $\Sigma = \text{diag}(\sigma_1, \dots, \sigma_m)$, $z \sim \mathcal{N}(0, I_m)$ and $\mathcal{M}(x_0)_i = \langle a \Delta^i, x_0^b \rangle$. We compute $\{\Delta^i\}_{i=1}^m$ by adapting Siddon’s ray-tracing algorithm (Siddon, 1985); see Appendix D for details. Therefore, the

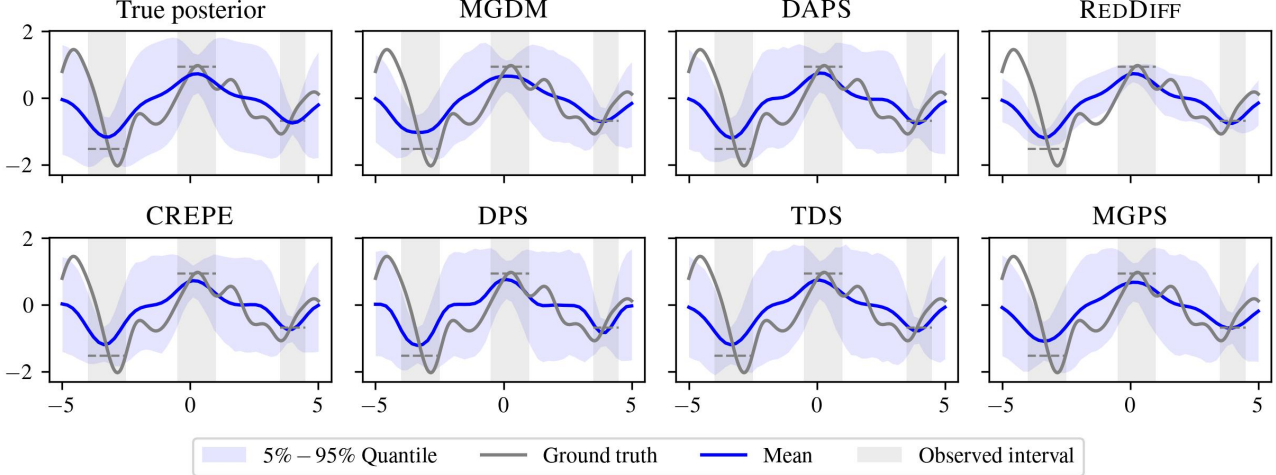


Figure 3. Comparison between the reconstructions of the baselines on the inverse problem with diffusion prior on the setting of GP. The y-axis shows intensities while the x-axis represents a one-dimensional grid of the $[-5, 5]$ interval. The dashed horizontal lines depict values of the integral over the observed intervals.

likelihood of the inverse problem is

$$p(y | x_0) \propto \exp\left\{-\frac{1}{2}\|y - \mathcal{M}(x_0)\|_{\Sigma^{-2}}^2\right\}, \quad (5)$$

with $\|v\|_{\Sigma^{-2}}^2 := v^\top \Sigma^{-2} v$. While the operator \mathcal{M} is nonlinear in x_0 , it is linear in the transformed variable $u = x_0^b$.

Training-Free Posterior Sampling with DM Priors. In training-free posterior sampling, the goal is, given measurements y , sample from the posterior distribution

$$\pi_0(x_0 | y) \propto p(y | x_0) p_0(x_0), \quad (6)$$

where p_0 is the implicit prior induced by a pre-trained DM. Let $\{\pi_t\}_{t=0}^T$ be the marginals obtained by applying the same corruption process $q_{t|0}(\cdot | x_0)$, as defined in (2), to $\pi_0(\cdot | y)$. Then the posterior reverse transitions satisfy

$$\begin{aligned} \pi_{t|t+1}(x_t | x_{t+1}, y) &\propto p_t(y | x_t) p_{t|t+1}(x_t | x_{t+1}), \quad (7) \\ \text{where } p_t(y | x_t) &= \mathbb{E}_{x_0 \sim p_{0|t}(\cdot | x_t)} [p(y | x_0)], \end{aligned}$$

see Janati et al. (2025b, Eq. 1.18). The intermediate likelihoods $p_t(y | x_t)$ are typically intractable, as they involve an expectation of the likelihood under the denoising posterior distribution $p_{0|t}(x_0 | x_t)$, which is costly to sample.

A common approximation, introduced and used in the seminal work of Chung et al. (2023) replaces the full posterior expectation in (7) with a point estimate: one plugs the denoiser $D_t(x_t)$ into the likelihood; *i.e.*

$$p_t(y | x_t) \approx p_0(y | D_t(x_t)),$$

and uses the resulting gradient to guide sampling, analogous to classifier guidance (Dhariwal & Nichol, 2021). This

approximation is exact when $p_{0|t}(\cdot | x_t)$ concentrates at a single point which holds approximately at low noise levels but deteriorates as σ_t increases.

Alternatively, several approaches have been proposed to alleviate the problem of intractability using different approximations. *Score-based methods* (Song et al., 2022) modify the reverse SDE by adding a user-chosen likelihood score term. *Projection methods*, such as DDRM (Kawar et al., 2022), exploit the special structure in linear Gaussian inverse problems. *Variational approaches* (Mardani et al., 2024; Moufad et al., 2025; Janati et al., 2025a) use different approximation of $p_t(y | x_t)$ together with variational inference to approximate either the posterior π_0 in (6) (e.g., with a Gaussian) (Mardani et al., 2024), or the posterior transitions (Moufad et al., 2025; Janati et al., 2025a). *Sequential Monte Carlo (SMC)* approximates the sequence of posterior distributions $\{\pi_t(\cdot | y)\}_{t=0}^T$ using a population of weighted particles (Del Moral et al., 2006; Chopin et al., 2020). Unlike variational approaches that evolve a single solution, SMC propagates and reweights N particles, thereby maintaining a population-based representation of the posterior. *Replica Exchange* constructs a Markov chain targeting the product distribution $\bigotimes_{t=0}^T \pi_t(\cdot | y)$. Each iteration alternates between two types of updates: (i) *local moves*, which independently target the marginals $\pi_t(\cdot | y)$ and can be executed in parallel, and (ii) *communication moves*, which propose Metropolis–Hastings swaps between neighboring states (t_{m-1}, t_m) . In He et al. (2025b), the communication step departs from standard swap proposals by instead proposing new states. Since the resulting acceptance ratio involves the prior marginal density, He et al. (2025b) relies on the estimator of He et al. (2025a), which computes density ratios via the forward and the surrogate

reverse processes.

We refer to Daras et al. (2024); Janati et al. (2025b) for detailed survey on the landscape of methods for training-free posterior sampling with DM priors.

5. Experiments

Experimental Settings. We conduct (i) simulated and controlled experiments based on GP prior (Rasmussen & Williams, 2006), and (ii) real-world experiments on the OpenMRG dataset (Andersson et al., 2022; Fencl et al., 2024). In our target setting, CMLs are the primary source of observations. Hence, we consider as classical baselines IDW, GMZ, and OK, whereas RM is not applicable because it requires rain-gauge measurements to estimate the marginal distributions used by the method.

Meteorological Baselines. We briefly revisit the principles behind the baselines used in rain field reconstruction.

Inverse Distance Weighting (IDW). In IDW, the path-integrated observations of CMLs are converted into VRGs at the middle of the links. The rain rate at location \mathbf{s} is estimated as a weighted average of nearby observations

$$\hat{X}(\mathbf{s}) = \sum_{i=1}^N w_i(\mathbf{s}) X(\mathbf{s}_i), \quad w_i(\mathbf{s}) = d_i^{-p} / \sum_{j=1}^N d_j^{-p},$$

where $X(\mathbf{s}_i)$ is the rainfall intensity associated with the i -th VRG positioned at location \mathbf{s}_i , $d_i = \|\mathbf{s} - \mathbf{s}_i\|$ is the distance to \mathbf{s}_i , and $p > 0$ controls the decay of influence with distance.

GMZ algorithm. Rather than representing each CML by a single VRGs at its midpoint, the GMZ algorithm accounts for the variability of the rainfall rate along the CML link considering K VRGs evenly distributed along the CML link. More precisely, for the CML link \mathcal{L}_i , the K VRGs are positioned at $\{\mathbf{s}_{i,k}\}_{k=1}^K$, and the rain intensity at the latter points is constrained to match the observation $Y_i = \frac{a}{K} \sum_{k=1}^K X_{\ell,k}^b$. This redistribution is performed iteratively using neighboring links to enforce spatial consistency, and the resulting VRGs are interpolated with IDW (Goldshstein et al., 2009).

Ordinary Kriging (OK). Similar to IDW, OK uses the VRG simplification of the path-integrated measurement. OK uses GP prior with user-defined kernel (variogram) as an assumption over the rain field to interpolate the observations. The prior parameters are chosen by minimizing the L1 norm (Matheron, 1963a; Cressie, 1993a).

Diffusion Baselines. We select seven training-free posterior sampling baselines that represent the approach presented in Section 4, namely, DPS (Chung et al., 2023), DAPS (Zhang et al., 2024), REDDIFF (Mardani et al., 2024),

CREPE (He et al., 2025b), MGPS (Moufad et al., 2025), MGDM (Janati et al., 2025a), TDS (Wu et al., 2023).

We provide details on the implementation of both meteorological and Diffusion baselines as well as hyperparameter choices in Section C. When reporting results, we highlight the best metric with and second best .

While CREPE is included in the Gaussian process experiments, we exclude it from the CML experiments. In this setting, the method exhibits substantially higher computational cost than the other baselines and yields moderate performance. For these reasons, we omit CREPE from both the quantitative results and qualitative comparisons.

5.1. Simulated Examples

We consider a one-dimensional linear inverse problem where the latent field is a Gaussian process $X \sim \mathcal{GP}(0, k)$ on $[-5, 5]$, with an RBF kernel

$$k(s, s') = \exp\left(-\frac{(s - s')^2}{2\ell^2}\right), \quad \ell = 0.6. \quad (8)$$

The links $\{\mathcal{L}_i\}_{i=1}^m$ in this setting reduce to intervals $\{[a_i, b_i]\}_{i=1}^m$ ², and the observation model

$$Y_i = \int_{a_i}^{b_i} X(s) ds + \sigma Z_i, \quad Z_i \sim \mathcal{N}(0, 1), \quad (9)$$

where $\{Z_i\}_{i=1}^m$ are mutually independent and independent of X . Because the observation operator is linear and the prior is Gaussian, the posterior is a GP with closed-form mean and covariance (Rasmussen & Williams, 2006):

$$\mu_{X|y}(s) = \mathbf{k}_y(s)^\top (\mathbf{K}_{yy} + \sigma^2 \mathbf{I})^{-1} \mathbf{y},$$

$$k_{X|y}(s, s') = k(s, s') - \mathbf{k}_y(s)^\top (\mathbf{K}_{yy} + \sigma^2 \mathbf{I})^{-1} \mathbf{k}_y(s'),$$

where $\mathbf{k}_y(s)$ is a vector in \mathbb{R}^m with coordinates $[\mathbf{k}_y(s)]_i = \int_{a_i}^{b_i} k(s, s') ds'$, and \mathbf{K}_{yy} is a matrix in $\mathbb{R}^{m \times m}$ with elements $[\mathbf{K}_{yy}]_{ij} = \int_{a_i}^{b_i} \int_{a_j}^{b_j} k(s, s') ds ds'$. In our case, we postpone the derivations of these formulas to Section E. We discretize the interval $[-5, 5]$ into 50 points. Evaluating the Gaussian process X on this grid yields a multivariate Gaussian distribution. Consequently, for training-free baselines, we employed a DM prior to targeting this Gaussian distribution. Such a DM admits a closed-form construction, as described in Moufad et al. (2025, Appendix B).

Evaluation. This setting provides an oracle posterior, enabling a precise evaluation. We report (i) the sliced Wasserstein distance between the true and approximate posteriors (Rabin et al., 2011; Bonneel et al., 2015), and (ii) ℓ_2 errors between the oracle and the approximate quantities: posterior mean and the 5%-95% pointwise quantiles.

²In the GP experiments, we abuse the notation and use a_i and b_i to denote integration intervals instead of the power-law constants.

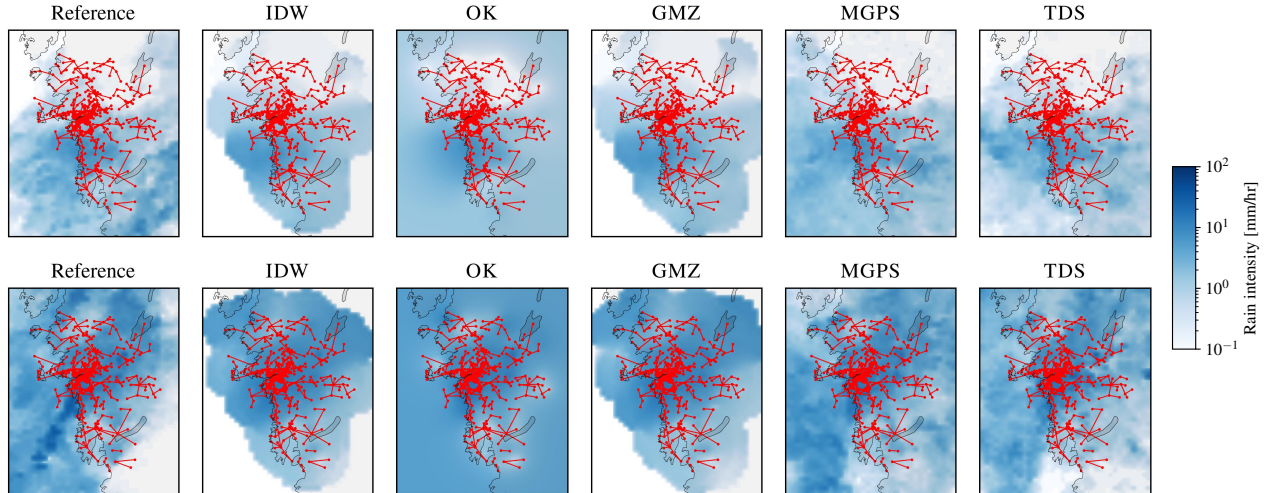


Figure 4. Comparisons of rain field reconstructions on real CMLs links from OpenMRG. We depict the network of CMLs in red.

Table 1. Quantitative comparison between Diffusion Models baselines on GP experiment. First row reports Sliced Wasserstein distance. The last 3 rows report ℓ_2 distance between reference and approximate mentioned quantity. Lower metrics are better.

	MGDM	DAPS	REDDIFF	CREPE	DPS	TDS	MGPS
SW ↓	0.16	0.09	0.38	0.13	0.12	0.07	0.09
Mean ↓	0.61	0.54	0.36	0.68	0.98	0.53	0.53
5%-Quantile ↓	2.21	1.12	5.70	1.82	1.17	0.85	0.99
95%-Quantile ↓	2.20	1.29	5.73	1.51	1.30	1.02	1.35

Results. The results are reported in Table 1. On the GP benchmark, TDS is the strongest overall method, achieving the best distributional match (lowest SW) and the most accurate uncertainty while remaining competitive on the mean. In contrast, REDDIFF achieves the lowest mean error but performs poorly on SW and tails, indicating that mean accuracy alone can mask severe posterior miscalibration. DAPS and MGPS perform competitively with moderate quantile errors. MGDM is generally less competitive, with a higher SW and substantially worse tail errors. We provide qualitative examples in Figures 3 and 7.

5.2. Real Dataset

We evaluate our approach on the OpenMRG dataset (Andersson et al., 2022) and use the Python package `PYNNcm1` (Habi, 2026; Chwala et al., 2026) to download and preprocess it. The dataset provides synchronized measurements from CMLs, weather radar, and RGs over the Gothenburg metropolitan area (Sweden) during June–August 2015.

Commercial Microwave Links. The network contains 364 bidirectional links (728 sub-links) operating at frequencies between 7 and 38 GHz (mostly above 25 GHz), with path lengths between 0.1 km and 15 km (median ≈ 2 km).

Transmitted and received signal levels are recorded every 10 seconds for each sub-link. Each link is associated with a pair of power-law parameters (a, b) (Eq. 1), whose dependence on frequency and path length is summarized in Figure 5.

Radar-derived Reference Fields. Radar data are drawn from the Swedish NORDRAD composite product operated by SMHI. The composite is generated from multiple Swedish radars using the Rainbow software and provides reflectivity fields on a 2 km grid; coverage over Gothenburg is primarily from the Vara radar (at ≈ 78 km), with partial contributions from nearby radars. The product is gauge-corrected using a distance-dependent gauge-radar ratio estimation (Michelson & Koistinen, 2000). Reflectivity is expressed in dBZ and stored as pseudo-dBZ values, which are converted back to actual dBZ before processing; values are then mapped to linear units and converted to rainfall intensity via a standard Z - R power-law relationship commonly used for stratiform conditions.

Evaluation. Since spatially dense ground truth is not directly observed, we use the gauge-adjusted radar-derived rain-rate fields as reference maps for evaluation. Attenuation observations are generated by applying the CML observation operator to radar rain-rate fields from the test split, using the OpenMRG network topology, link lengths, and link-specific power-law parameters (a_i, b_i) . We consider two noise settings: **1** *Isotropic noise* where all CML observations are corrupted with the same noise level σ and **2** *Heteroscedastic noise*, where the noise level depends on the CML length. Specifically, for link i with length L_i , we set $\sigma_i = \frac{\sigma}{2} \left(1 + \frac{L_i}{L_{\max}} \right)$, so that longer links have larger noise levels, with $\sigma_i = \sigma$ when $L_i = L_{\max}$ and $\sigma/2 \leq \sigma_i < \sigma$ otherwise. Note that other heteroscedastic noise models

could also be considered. Such settings can be incorporated straightforwardly by specifying the covariance matrix Σ of the observation operator in Equation (5).

Metrics. Existing studies commonly rely on standard pixel-wise reconstruction metrics (Graf et al., 2021; Zhang et al., 2023). In our assessment, we report the root mean square error (RMSE), which quantifies the discrepancy between ground-truth and reconstructed fields, and the Pearson correlation coefficient (PCC), which measures their linear agreement. We also evaluate the error in cumulative rainfall, defined as the difference between the total precipitation of the reconstructed and ground-truth fields. Values closer to zero indicate better agreement, with positive values corresponding to overestimation and negative values to underestimation of total rainfall. For computational reasons, we restrict the maximum runtime of the diffusion baselines to 3 minutes. For TDS, this requires reducing the number of particles to satisfy the runtime constraint. Hyperparameter details for all baselines are provided in Table 7.

Results. Table 3 shows that the diffusion-model baselines consistently outperform the meteorological baselines across both settings and evaluation metrics. In particular, MGPS achieves strong performance on all three metrics. Overall, DM-based reconstructions exhibit higher agreement with the reference fields, as reflected by their PCC values. Among the meteorological methods, GMZ performs well in terms of cumulative rainfall, while OK yields the strongest overall performance within this class of baselines. The results under heterogeneous noise are slightly better, as expected, since this setting has a lower overall noise level.

Qualitative comparisons are provided in Figure 4, with a detailed comparison including all methods in Figures 8 and 9.

Runtime. To assess computational cost, we report the runtimes of the meteorological and diffusion-based baselines in Table 2. The results highlight a trade-off: meteorological methods are fast but they (except OK) produce a deterministic reconstruction; the diffusion baselines are more expensive yet they generate ensembles of plausible rain fields. This enables the assessment of multiple scenarios, including best- and worst-case precipitation patterns that may be relevant for flood-warning applications.

Table 2. Runtime (in seconds) per reconstruction for all baselines. For diffusion-based methods, the reported runtime is divided by 10, since a batch of 10 samples is generated jointly.

	DAPS	DPS	MGDM	MGPS	REDDIFF	TDS	IDW	GMZ	OK
Runtime	6.06	5.27	6.87	5.22	5.95	18.49	0.01	1.01	0.27

In our experiments, generating 10 samples with the diffusion baselines takes roughly one minute. Since CML data is

Table 3. Comparison between DM and meteorological baselines on RMSE, PCC, and difference of Cumulative Rain on real CML links from OpenMRG. 95%-confidence intervals are shown.

	RMSE ↓	PCC ↑	Cumulative Rain → 0
Isotropic noise			
DAPS	0.88 ± 0.09	0.24 ± 0.02	-320 ± 53.66
DPS	0.88 ± 0.09	0.20 ± 0.01	-333 ± 54.34
MGDM	0.91 ± 0.08	0.22 ± 0.02	231 ± 35.29
MGPS	0.86 ± 0.08	0.24 ± 0.01	42 ± 34.65
REDDIFF	0.86 ± 0.09	0.23 ± 0.02	-356 ± 48.47
TDS	0.84 ± 0.09	0.21 ± 0.02	-216 ± 35.89
IDW	0.90 ± 0.09	0.21 ± 0.01	-144 ± 32.26
GMZ	0.92 ± 0.09	0.21 ± 0.01	-65 ± 29.26
OK	0.87 ± 0.09	0.23 ± 0.02	158 ± 38.67
Heteroscedastic noise			
DAPS	0.87 ± 0.10	0.24 ± 0.01	-438.80 ± 76.08
DPS	0.85 ± 0.09	0.21 ± 0.01	-349.25 ± 53.49
MGDM	0.92 ± 0.08	0.24 ± 0.01	300.00 ± 36.24
MGPS	0.83 ± 0.08	0.26 ± 0.01	70.94 ± 36.40
REDDIFF	0.84 ± 0.09	0.24 ± 0.02	-370.92 ± 48.78
TDS	0.81 ± 0.09	0.25 ± 0.02	-241.43 ± 35.03
IDW	0.86 ± 0.09	0.24 ± 0.01	-166.95 ± 32.09
GMZ	0.91 ± 0.09	0.21 ± 0.01	-81.93 ± 29.09
OK	0.86 ± 0.09	0.24 ± 0.02	140.74 ± 38.83

aggregate at intervals of 5 to 15 minutes, these runtimes remain compatible with real-time meteorological monitoring.

5.3. Ablation

DM Prior and Nonlinear Observation Model. We first disentangle the gains due to the diffusion prior from those due to accurate modeling of the nonlinear path-integrated observation operator. To this end, we consider an ablation in which observations are generated under the true nonlinear setting, with power law $b_i > 1$, while inference assumes $b_i = 1$, yielding a linear observation model. To assess the role of the diffusion prior quality, we repeat this experiment with both a “Strong” and a “Weak” prior; the latter corresponding to an undertrained diffusion model trained for a small number of epochs. Results are reported in Table 5.

Discussion. The results show that the diffusion prior improves the reconstructed rain fields; with accurate modeling of the nonlinear observation operator being essential for strong quantitative performance.

CML Network Configuration. We next assess the impact of CML network geometry, focusing on the number and spatial configuration of links. We consider two synthetic configurations: a *few-long* setting with 25 long CMLs and a *many-short* setting with 100 short CMLs. To isolate the effect of spatial configuration, we restrict this ablation to the case where the power-law exponent is equal to 1, resulting in a linear inverse problem. Results are reported in Table 4.

Table 4. Ablation between DMs and meteorological baselines on RMSE, PCC, and difference of Cumulative Rain (Cum Rain). Two settings are considered on OpenMRG dataset with simulated CMLs: few-long and many-short links, with the power-law $b = 1$. For RMSE lower is better. For PCC, higher is better. For Cum Rain, closer to 0 is better.

	Few-long links			Many-short links		
	RMSE ↓	PCC ↑	Cum Rain	RMSE ↓	PCC ↑	Cum Rain
DAPS	0.92	0.24	-243	1.16	0.29	-348
DPS	0.88	0.23	-267	0.80	0.32	-152
MGDM	0.89	0.25	152	0.79	0.38	153
MGPS	0.84	0.28	11	0.75	0.41	20
REDDIFF	0.85	0.26	-221	0.79	0.37	-224
TDS	0.85	0.23	-163	0.76	0.34	-77
IDW	0.89	0.25	-164	0.75	0.42	3
GMZ	0.86	0.29	-20	0.75	0.43	15
OK	0.83	0.28	19	0.76	0.38	27

Discussion. In this idealized linear setting, meteorological baselines perform comparably to DM-based methods, with OK achieving the lowest RMSE. This suggests that, under linear sensing and sufficiently dense coverage, the rainfall field can be well approximated by a Gaussian-process model and effectively reconstructed by interpolation. Meteorological baselines further benefit from increased CML density, particularly when links are well distributed across the domain, as shown in Table 4.

Real-world CML observations, however, deviate substantially from this regime. As shown in Figure 5, the power-law exponent b varies over a wide range, inducing nonlinear measurements. Moreover, operational CML networks are typically spatially heterogeneous, with dense coverage in some regions and sparse or absent coverage in others, as illustrated in Figure 4. These factors highlight the limitations of interpolation-based meteorological baselines and motivate the use of expressive priors coupled with physically grounded observation models, as in the proposed DM-based framework.

Table 5. Ablation to discern the improvement that comes from the DM prior vs. the improvement from accounting for the nonlinearity of the measurement operator. “Weak-prior” is an under-trained DM, i.e. a DM trained with very-few number epochs.

DM	Sampler	Linear operator			Nonlinear operator		
		RMSE ↓	PCC ↑	Cum Rain → 0	RMSE ↓	PCC ↑	Cum Rain → 0
Weak	MGPS	0.94	0.17	-430.30	0.88	0.23	132.21
	REDDIFF	1.01	0.16	-661.38	0.90	0.19	-456.52
	TDS	0.96	0.11	-543.51	0.86	0.18	-259.54
Strong	MGPS	0.96	0.16	-436.11	0.86	0.24	42.86
	REDDIFF	1.00	0.17	-643.39	0.86	0.23	-356.76
	TDS	0.97	0.13	-549.76	0.84	0.21	-216.44

6. Conclusion

We presented a Bayesian framework for rain field reconstruction from CMLs that leverages DMs as expressive spatial priors. Formulating the problem as a Bayesian inverse prob-

lem enables training-free posterior sampling using a wide range of modern inference methods. Crucially, the proposed framework incorporates a physically grounded measurement operator that accounts for the path-integrated nature of CML observations, moving beyond the VRG assumption.

Limitations and Future Work. The DM prior is trained on data from a single geographic region and season. Its performance under distribution shift to other climates and meteorological regimes has not been assessed. Moreover, our current formulation treats rainfall fields independently across time, thereby neglecting temporal structure. Future work will explore spatiotemporal modeling extensions to address these limitations.

Impact Statement

The proposed approach may contribute to the monitoring of hydric resources by enabling more effective use of opportunistic sensing data, and may support urban flood and hazard prevention through improved rainfall estimation. At the same time, because opportunistic sensing relies on telecommunications infrastructure, its deployment may introduce user exposure and privacy-related risks that warrant careful consideration. These potential impacts should be taken into account when translating such methods into operational systems.

Acknowledgements

The work of Badr Moufad has been supported by Technology Innovation Institute (TII), project Fed2Learn. The work of Eric Moulines has been partly funded by the European Union (ERC-2022-SYG-OCEAN-101071601). Views and opinions expressed are however those of the author(s) only and do not necessarily reflect those of the European Union or the European Research Council Executive Agency. Neither the European Union nor the granting authority can be held responsible for them. This work was granted access to the HPC resources of IDRIS under the allocations 2025-AD011015980 made by GENCI.

References

- Ailliot, P., Thompson, C., and Thomson, P. Space-time modelling of precipitation by using a hidden markov model and censored gaussian distributions. *Journal of the Royal Statistical Society Series C: Applied Statistics*, 58(3):405–426, 2009.
- Andersson, J. C., Olsson, J., Van de Beek, R., and Hansryd, J. Openmrp: Open data from microwave links, radar, and gauges for rainfall quantification in gothenburg, sweden. *Earth System Science Data*, 14(12):5411–5426, 2022.

- Bardossy, A. and Plate, E. J. Space-time model for daily rainfall using atmospheric circulation patterns. *Water resources research*, 28(5):1247–1259, 1992.
- Baxevani, A. and Lennartsson, J. A spatiotemporal precipitation generator based on a censored latent gaussian field. *Water Resources Research*, 51(6):4338–4358, 2015.
- Blettner, N., Chwala, C., Haese, B., Hörning, S., and Kunstmann, H. Combining commercial microwave link and rain gauge observations to estimate countrywide precipitation: A stochastic reconstruction and pattern analysis approach. *Water Resources Research*, 58(10):e2022WR032563, 2022.
- Bonneel, N., Rabin, J., Peyré, G., and Pfister, H. Sliced and radon wasserstein barycenters of measures. *Journal of Mathematical Imaging and Vision*, 2015.
- Botev, Z. I. The normal law under linear restrictions: simulation and estimation via minimax tilting. *Journal of the Royal Statistical Society Series B: Statistical Methodology*, 79(1):125–148, 2017.
- Cappé, O., Moulines, E., and Rydén, T. *Inference in hidden Markov models*. Springer, 2005.
- Chopin, N., Papaspiliopoulos, O., et al. *An introduction to sequential Monte Carlo*, volume 4. Springer, 2020.
- Chung, H., Kim, J., Mccann, M. T., Klasky, M. L., and Ye, J. C. Diffusion posterior sampling for general noisy inverse problems. In *The Eleventh International Conference on Learning Representations*, 2023. URL <https://openreview.net/forum?id=OnD9zGAGT0k>.
- Chwala, C., Overeem, A., Øydvin, E., Petersson Wårdh, L., Seidel, J., Graf, M., Walraven, B., Covi, E., Habi, H. V., Fencel, M., et al. Open-source tools for processing opportunistic rainfall sensor data: An overview of existing tools and the new opensense software packages poligrain, pypwsqc and mergeplg. *EGU sphere*, 2026:1–31, 2026.
- Cressie, N. A. C. *Statistics for Spatial Data*. Wiley, 1993a. Revised edition.
- Cressie, N. A. C. *Statistics for Spatial Data*. Wiley, 1993b.
- Daras, G., Chung, H., Lai, C.-H., Mitsufuji, Y., Ye, J. C., Milanfar, P., Dimakis, A. G., and Delbraccio, M. A survey on diffusion models for inverse problems. *arXiv preprint arXiv:2410.00083*, 2024.
- Del Moral, P., Doucet, A., and Jasra, A. Sequential monte carlo samplers. *Journal of the Royal Statistical Society: Series B (Statistical Methodology)*, 68(3):411–436, 2006. doi: <https://doi.org/10.1111/j.1467-9868.2006.00553.x>. URL <https://rss.onlinelibrary.wiley.com/doi/abs/10.1111/j.1467-9868.2006.00553.x>.
- Dhariwal, P. and Nichol, A. Diffusion models beat gans on image synthesis. *Advances in neural information processing systems*, 34:8780–8794, 2021.
- Eshel, A., Messer, H., Kunstmann, H., Alpert, P., and Chwala, C. Quantitative analysis of the performance of spatial interpolation methods for rainfall estimation using commercial microwave links. *Journal of Hydrometeorology*, 22(4):831–843, 2021.
- Fencel, M., Nebuloni, R., Andersson, J. C., Bares, V., Blettner, N., Cazzaniga, G., Chwala, C., Colli, M., de Vos, L., El Hachem, A., et al. Data formats and standards for opportunistic rainfall sensors. *Open Research Europe*, 3:169, 2024.
- Funk, C. C., Peterson, P. J., Landsfeld, M. F., Pedreros, D. H., Verdin, J. P., Rowland, J. D., Romero, B. E., Husak, G. J., Michaelsen, J. C., and Verdin, A. P. A quasi-global precipitation time series for drought monitoring. Report, U.S. Geological Survey, 2014.
- Goldshstein, O., Messer, H., and Zinevich, A. Rain rate estimation using measurements from commercial telecommunications links. *IEEE Transactions on Signal Processing*, 57(4):1616–1625, 2009. doi: 10.1109/TSP.2009.2012554.
- Graf, M., Chwala, C., Polz, J., and Kunstmann, H. Rainfall estimation from a german-wide commercial microwave link network: optimized processing and validation for 1 year of data. *Hydrology and Earth System Sciences*, 24(6):2931–2950, 2020.
- Graf, M., El Hachem, A., Eisele, M., Seidel, J., Chwala, C., Kunstmann, H., and Bárdossy, A. Rainfall estimates from opportunistic sensors in germany across spatio-temporal scales. *Journal of Hydrology: Regional Studies*, 37:100883, 2021.
- Graf, M., Bareš, V., Messer, H., Nebuloni, R., Fencel, M., Chwala, C., Overeem, A., Van de Beek, R., Olsson, J., Ostrometzky, J., et al. The opportunistic precipitation sensing network (opensense). *Bulletin of the American Meteorological Society*, 107(3):E585–E591, 2026.
- Habi, H. V. Pynncml: Rain estimation and classification from commercial microwave links data, 2026. URL <https://github.com/haihabi/PyNNcml>.
- Habi, H. V. and Messer, H. Raingan: A conditional rain fields generator. In *2021 IEEE International Conference on Microwaves, Antennas, Communications and Electronic Systems (COMCAS)*, pp. 529–532. IEEE, 2021.

- Haese, B., Hörning, S., Chwala, C., Bárdossy, A., Schalge, B., and Kunstmann, H. Stochastic reconstruction and interpolation of precipitation fields using combined information of commercial microwave links and rain gauges. *Water Resources Research*, 53(12):10740–10756, 2017.
- Harrison, D., Driscoll, S., and Kitchen, M. Improving precipitation estimates from weather radar using quality control and correction techniques. *Meteorological Applications*, 7(2):135–144, 2000.
- He, J., Hernández-Lobato, J. M., Du, Y., and Vargas, F. Rne: a plug-and-play framework for diffusion density estimation and inference-time control. *arXiv preprint arXiv:2506.05668*, 2025a.
- He, J., Jeha, P., Potapchik, P., Zhang, L., Hernández-Lobato, J. M., Du, Y., Syed, S., and Vargas, F. Crepe: Controlling diffusion with replica exchange. *arXiv preprint arXiv:2509.23265*, 2025b.
- Ho, J., Jain, A., and Abbeel, P. Denoising diffusion probabilistic models. *Advances in Neural Information Processing Systems*, 33:6840–6851, 2020.
- Hörning, S., Sreekanth, J., and Bárdossy, A. Computational efficient inverse groundwater modeling using random mixing and whittaker–shannon interpolation. *Advances in Water Resources*, 123:109–119, 2019.
- International Telecommunication Union. Recommendation ITU-R P.838-3: Specific attenuation model for rain for use in prediction methods. Technical Report P.838-3, ITU-R, March 2005. URL <https://www.itu.int/rec/R-REC-P.838-3-200503-I/en>. Approved in March 2005.
- Janati, Y., Moufad, B., Abou El Qassime, M., Durmus, A. O., Moulines, E., and Olsson, J. A mixture-based framework for guiding diffusion models. In *Forty-second International Conference on Machine Learning*, 2025a.
- Janati, Y., Moulines, E., Olsson, J., and Oliviero-Durmus, A. Bridging diffusion posterior sampling and monte carlo methods: a survey. *Philosophical Transactions A*, 383(2299):20240331, 2025b.
- Karras, T., Aittala, M., Aila, T., and Laine, S. Elucidating the design space of diffusion-based generative models. *Advances in Neural Information Processing Systems*, 35:26565–26577, 2022.
- Kawar, B., Elad, M., Ermon, S., and Song, J. Denoising diffusion restoration models. *Advances in Neural Information Processing Systems*, 35:23593–23606, 2022.
- Kingma, D. P. and Ba, J. Adam: A method for stochastic optimization. *arXiv preprint arXiv:1412.6980*, 2014.
- Krajewski, W. and Smith, J. Radar hydrology: rainfall estimation. *Advances in Water Resources*, 25(8):1387–1394, 2002. ISSN 0309-1708. doi: [https://doi.org/10.1016/S0309-1708\(02\)00062-3](https://doi.org/10.1016/S0309-1708(02)00062-3). URL <https://www.sciencedirect.com/science/article/pii/S0309170802000623>.
- Leijnse, H., Uijlenhoet, R., and Stricker, J. Rainfall measurement using radio links from cellular communication networks. *Water resources research*, 43(3), 2007.
- Lopez-Paz, D. and Oquab, M. Revisiting classifier two-sample tests. *arXiv preprint arXiv:1610.06545*, 2016.
- Mardani, M., Song, J., Kautz, J., and Vahdat, A. A variational perspective on solving inverse problems with diffusion models. In *The Twelfth International Conference on Learning Representations*, 2024. URL <https://openreview.net/forum?id=1YO4EE3SPB>.
- Matheron, G. Principles of geostatistics. *Economic Geology*, 58(8):1246–1266, 1963a. doi: 10.2113/gsecongeo.58.8.1246.
- Matheron, G. Principles of geostatistics. *Economic Geology*, 58(8):1246–1266, 1963b. doi: 10.2113/gsecongeo.58.8.1246. URL <https://doi.org/10.2113/gsecongeo.58.8.1246>.
- Messer, H., Zinevich, A., and Alpert, P. Environmental monitoring by wireless communication networks. *Science*, 312(5774):713–713, 2006.
- Messer, H., Eshel, A., Habi, H., Sagiv, S., and Zheng, X. Rain field retrieval by ground-level sensors of various types. *Frontiers in Signal Processing*, 2:877336, 2022.
- Michelson, D. and Koistinen, J. Gauge-radar network adjustment for the baltic sea experiment. *Physics and Chemistry of the Earth, Part B: Hydrology, Oceans and Atmosphere*, 25(10):915–920, 2000. ISSN 1464-1909. doi: [https://doi.org/10.1016/S1464-1909\(00\)00125-8](https://doi.org/10.1016/S1464-1909(00)00125-8). URL <https://www.sciencedirect.com/science/article/pii/S1464190900001258>. First European Conference on Radar Meteorology.
- Moufad, B., Janati, Y., Bedin, L., Durmus, A. O., randal douc, Moulines, E., and Olsson, J. Variational diffusion posterior sampling with midpoint guidance. In *The Thirteenth International Conference on Learning Representations*, 2025. URL <https://openreview.net/forum?id=6EUtjXAvmj>.
- Murphy, B., Yurchak, R., and Müller, S. Geostat-framework/pykrige: v1.7.3, oct 2025. URL <https://doi.org/10.5281/zenodo.17372225>.

- Nichol, A. Q. and Dhariwal, P. Improved denoising diffusion probabilistic models. In Meila, M. and Zhang, T. (eds.), *Proceedings of the 38th International Conference on Machine Learning*, volume 139 of *Proceedings of Machine Learning Research*, pp. 8162–8171. PMLR, 18–24 Jul 2021. URL <https://proceedings.mlr.press/v139/nichol21a.html>.
- Ordoñez, J. A., Bandyopadhyay, D., Lachos, V. H., and Cabral, C. R. B. Geostatistical estimation and prediction for censored responses. *Spatial Statistics*, 23:109–123, 2018. doi: 10.1016/j.spasta.2017.12.001.
- Overeem, A., Leijnse, H., and Uijlenhoet, R. Country-wide rainfall maps from cellular communication networks. *Proceedings of the National Academy of Sciences*, 110(8): 2741–2745, 2013.
- Overeem, A., Leijnse, H., and Uijlenhoet, R. Retrieval algorithm for rainfall mapping from microwave links in a cellular communication network. *Atmospheric Measurement Techniques*, 9(5):2425–2444, 2016.
- Pakman, A. and Paninski, L. Exact hamiltonian monte carlo for truncated multivariate gaussians. *Journal of Computational and Graphical Statistics*, 23(2):518–542, 2014.
- Pasierb, M., Bałdysz, Z., Szturc, J., Nykiel, G., Jurczyk, A., Ośródk, K., Figurski, M., Wojtczak, M., and Wojtkowski, C. Application of commercial microwave links (cmls) attenuation for quantitative estimation of precipitation. *Meteorological Applications*, 31(3):e2218, 2024.
- Rabin, J., Peyré, G., Delon, J., and Bernot, M. Wasserstein barycenter and its application to texture mixing. In *Scale Space and Variational Methods in Computer Vision (SSVM)*. Springer, 2011.
- Rasmussen, C. E. and Williams, C. K. Gaussian processes for machine learning. *Cambridge, MA, USA: Massachusetts Institute of Technology Publishing*, 2006.
- Shepard, D. A two-dimensional interpolation function for irregularly-spaced data. In *Proceedings of the 1968 23rd ACM national conference*, pp. 517–524, 1968.
- Siddon, R. L. Fast calculation of the exact radiological path for a three-dimensional ct array. *Medical physics*, 12(2): 252–255, 1985.
- Song, J., Meng, C., and Ermon, S. Denoising diffusion implicit models. In *International Conference on Learning Representations*, 2021a. URL <https://openreview.net/forum?id=St1gjarCHLP>.
- Song, Y., Sohl-Dickstein, J., Kingma, D. P., Kumar, A., Ermon, S., and Poole, B. Score-based generative modeling through stochastic differential equations. In *International Conference on Learning Representations*, 2021b.
- Song, Y., Shen, L., Xing, L., and Ermon, S. Solving inverse problems in medical imaging with score-based generative models. In *International Conference on Learning Representations*, 2022. URL <https://openreview.net/forum?id=vaRCHVj0uGI>.
- Stauffer, R., Mayr, G. J., Messner, J. W., Umlauf, N., and Zeileis, A. Spatio-temporal precipitation climatology over complex terrain using a censored additive regression model. *International Journal of Climatology*, 37(7):3264–3275, 2017.
- Uijlenhoet, R., Overeem, A., and Leijnse, H. Opportunistic remote sensing of rainfall using microwave links from cellular communication networks. *Wiley Interdisciplinary Reviews: Water*, 5(4):e1289, 2018.
- Wheater, H., Isham, V., Cox, D., Chandler, R., Kakou, A., Northrop, P., Oh, L., Onof, C., and Rodriguez-Iturbe, I. Spatial-temporal rainfall fields: modelling and statistical aspects. *Hydrology and Earth System Sciences*, 4(4): 581–601, 2000.
- Wilks, D. S. and Wilby, R. L. The weather generation game: a review of stochastic weather models. *Progress in physical geography*, 23(3):329–357, 1999.
- Wu, L., Trippe, B., Naesseth, C., Blei, D., and Cunningham, J. P. Practical and asymptotically exact conditional sampling in diffusion models. *Advances in Neural Information Processing Systems*, 36:31372–31403, 2023.
- Yang, C., Chandler, R., Isham, V., and Wheeler, H. Spatial-temporal rainfall simulation using generalized linear models. *Water Resources Research*, 41(11), 2005.
- Zhang, B., Chu, W., Berner, J., Meng, C., Anandkumar, A., and Song, Y. Improving diffusion inverse problem solving with decoupled noise annealing. *arXiv preprint arXiv:2407.01521*, 2024.
- Zhang, P., Liu, X., and Zou, M. Reconstructing and nowcasting the rainfall field by a cml network. *Earth and Space Science*, 10(9):e2023EA002909, 2023. doi: <https://doi.org/10.1029/2023EA002909>. URL <https://agupubs.onlinelibrary.wiley.com/doi/abs/10.1029/2023EA002909>.

A. Extended Related Work

As discussed in Section 2, earlier studies on rainfall reconstruction from CMLs (Leijnse et al., 2007; Goldshtein et al., 2009; Overeem et al., 2013; 2016) typically reduced each path-integrated link observation to a VRG located at the link midpoint and then produced gridded rain fields via deterministic interpolation (most commonly IDW or OK). This abstraction enabled the first large-scale deployments of CML-based mapping, but it discards variability along the link and effectively converts line-integral measurements into point-scale information, which can yield overly smooth fields and miss localized extremes.

Recent work has systematically examined the implications of this approximation and the extent to which more faithful representations of CML measurements can improve reconstruction accuracy. Messer et al. (2022) quantify the information gain of line-integral observations relative to point measurements, demonstrating that CMLs contain additional spatial information that is lost when collapsed to a single point. Building on this insight, Eshel et al. (2021) evaluate rainfall reconstruction using a dense operational CML network in southern Germany and a semisynthetic framework based on gauge-adjusted radar data. Their results confirm that reconstruction accuracy strongly depends on rainfall spatial structure, improving for smoother fields with larger decorrelation distances. Importantly, they show that representing each CML by multiple VRGs using GMZ yields a consistent, though modest, improvement over the single-midpoint VRG representation, largely independent of whether IDW or OK is applied.

Similar conclusions emerge from other deterministic reconstruction analyses. Zhang et al. (2023) investigate two-dimensional rainfall fields reconstruction by converting attenuation measurements into path-averaged rain rates via power-law relationships and then interpolating them with IDW or OK. Their analysis shows that both methods recover the dominant spatial structures, with OK typically outperforming IDW due to its explicit modeling of spatial dependence. However, reconstruction quality deteriorates in sparsely covered regions and during high-intensity events, reflecting fundamental limitations imposed by network geometry and path integration. Moving beyond CML-only settings, Graf et al. (2021) demonstrate that jointly assimilating rain gauges, personal weather stations, and CMLs within a block-kriging framework substantially increases effective observation density and improves representation of spatial rainfall variability. Crucially, their approach accounts for differences in spatial support and sensor-specific uncertainties, yielding performance comparable to or exceeding gauge-adjusted radar at local and regional scales. Likewise, Pasierb et al. (2024) emphasize the sensitivity of CML-based reconstruction to link characteristics (e.g., length, frequency, orientation) as well as to the strategy used to project path-averaged measurements onto spatial grids, underscoring that preprocessing and mapping choices play a critical role in reconstruction quality.

While deterministic interpolation provides a single best estimate, it offer limited uncertainty quantification and may further oversmooth fine-scale variability when constraints are weak. To address these limitations, stochastic reconstruction approaches treat rainfall as a random spatial process conditioned on both point and path-integrated information. A key advance in this direction is the application of the RM framework by Haese et al. (2017), which generates an ensemble of rainfall fields that agree with rain gauges and with the path-averaged link measurements, so it keeps the fact that CMLs measure rainfall along a path rather than at a point. Compared to OK, RM can better preserve small-scale spatial variability and represent higher intensities (including extreme thresholds). However, because the marginal rainfall distribution is derived primarily from gauge data, RM remains sensitive to gauge representativeness and may underestimate extremes or delay rainfall onset when gauges inadequately sample localized events.

The RM framework has since been extended to larger spatial domains. Blettner et al. (2022) extend stochastic reconstruction to national domains by combining rain gauges and CMLs across an entire country, improving agreement with gauge-adjusted radar and reducing structural errors in rainfall pattern representation compared to deterministic kriging. Their uncertainty decomposition (amplitude, structure, location) highlights the diagnostic value of ensemble reconstructions. Nonetheless, increased computational cost, interpretative complexity, and the smoothing implied by path-integrated constraints continue to limit the recoverable resolution of fine-scale precipitation features, particularly where observational coverage is sparse.

B. Prior Diffusion Model

We base the prior model on the EDM framework (Karras et al., 2022) and adapt the publicly released implementation³ to our setting.

³<https://github.com/NVlabs/edm>

Dataset. The OpenMRG dataset contains 26,495 rain-rate fields, which are split chronologically into training and test sets with a 0.8/0.2 ratio, yielding 21,196 and 5,299 samples, respectively. Unlike the original EDM setup, we operate directly on rain-rate fields without converting them to PNG images. Each field has shape $(1, 48, 36)$; the width is cropped from 37 to 36 for consistency. To mitigate the long-tailed distribution of rainfall intensities, we experimented with two approaches:

Log-transform. We initially experimented with training on a log-transformed version of the rainfall data, which amounts to training a latent diffusion model where the encoder applies a log-transform and the decoder applies an exponential transform. While training in log-space was significantly faster (roughly $\times 1.5$), we ultimately opted against using the log-space model during inference. The primary reason is that mapping back to rain intensities via an exponential transform introduces an additional nonlinearity into the inverse problem. As noted in recent work on inverse problems with latent diffusion models, such nonlinearities can introduce numerical instabilities for diffusion samplers; in our case, the exp-transform led to instabilities for some of the diffusion baselines, namely for DPS and DAPS.

Linear-transform with quantiles. All samples are normalized by a fixed constant corresponding to the 0.999 quantile of the training data. We retained this as our final preprocessing choice: this linear normalization mitigates skewed values while preserving linearity in the input space, which we found more stable for inference.

Architecture. We use DDPM++ backbone (Song et al., 2021b) (SongUNet), a U-Net encoder–decoder with skip connections and timestep embeddings. The model uses `model_channels=32` and `dropout=0.1`. The denoiser is wrapped with EDM preconditioning (EDMPrecond) and $\sigma_{\text{data}} = 0.079$ is used in both the preconditioner and the EDM loss. A ReLU activation is applied to the denoiser output to enforce the physical constraint that the denoiser expectation $\mathbb{E}[X_0 | X_t]$ be non-negative.

Enforcing non-negative values. While the ReLU activation function is a valid heuristic to enforce non-negative values, it introduces a hard thresholding that can distort gradients near zero-intensity regions. We also experimented with a smoother alternative, namely the Softplus activation function⁴, which yields smoother gradients around zero. In practice, however, we found no significant difference in the performance of the diffusion prior between the two variants, indicating that our results are largely insensitive to whether non-negativity is enforced by a hard or smooth transformation.

Training Setup. Training is performed using Adam (Kingma & Ba, 2014) with $\beta_1 = 0.9$, $\beta_2 = 0.999$, and a constant learning rate of 10^{-4} for approximately 5,284 epochs. Data augmentation is limited to random axis flips, with each sample independently flipped along the x and y axes with probability 0.1. Exponential moving average updates are disabled. The training is conducted on two NVIDIA H100 (80GB) GPUs, with a total training time of approximately 10 hours.

Discriminator Training Details. The discriminator is trained as a supervised binary classifier to distinguish real from generated samples, with labels “1” and “0”, respectively. The two datasets are concatenated, randomly shuffled, and split into training and test sets using a 0.8/0.2 ratio. Optimization is performed using mini-batches of size 256.

The discriminator is a convolutional network operating on single-channel inputs of shape $(1, 48, 36)$. Its architecture follows Habi & Messer (2021) and consists of three convolutional blocks. Each block applies a 5×5 convolution with stride 2 and padding 2, followed by a LeakyReLU activation. Channel dimensions increase as $1 \rightarrow d \rightarrow 2d \rightarrow 4d$. The resulting feature maps are flattened and passed through a linear layer to produce a single logit.

Training minimizes the binary cross-entropy loss with logits using the Adam optimizer with a learning rate of 10^{-4} for 200 epochs. At evaluation time, predicted probabilities are thresholded at 0.5 to obtain class labels.

C. Baselines Implementation

In this section, we provide implementation details for all baseline methods against which we compare our approach. For the meteorological baselines, hyperparameters are presented in Table 6. The details about the hyperparameters of DM posterior samplers are summarized in Table 7. We highlight that all baseline hyperparameters were tuned manually. For completeness, we also report the runtime required to generate one reconstruction for each baseline in Table 2. The meteorological baselines are substantially faster than the diffusion baselines, for which the reported runtimes are normalized by batch size, since 10 samples are generated jointly and the total runtime is divided by 10 to obtain a per-reconstruction comparison.

⁴<https://docs.pytorch.org/docs/stable/generated/torch.nn.Softplus.html>

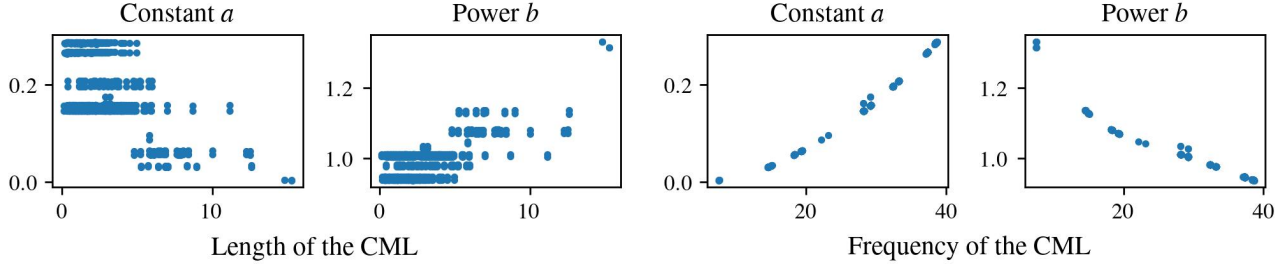


Figure 5. Power-law parameters of the CML as a function of link’s length and the frequency on the OpenMRG dataset.

C.1. Meteorological baselines

IDW. We implement inverse-distance weighting (IDW) following Eshel et al. (2021); Shepard (1968). Each CML link observation is represented as a point measurement located at the link midpoint. For every grid location s , we compute a normalized weighted average using $p = 2$ and $\epsilon = 10^{-6}$ for numerical stability. A region-of-influence radius roi is set to 4 in order to discard distant observations.

GMZ. We implement the iterative GMZ reconstruction procedure following Goldshtein et al. (2009); Eshel et al. (2021), that we adapt from PyNNcml (Habi, 2026). We first map each link measurement to the attenuation domain via the standard power law $A = aX^b$ (International Telecommunication Union, 2005). Each link is discretized into a fixed number of uniformly spaced VRGs. We use $K = 5$ virtual points per link and run the algorithm for $T = 20$ iterations. At each iteration, an intermediate field is reconstructed using the same IDW operator as in C.1. The reconstructed field is bilinearly sampled at the virtual points, and link consistency is enforced by projecting the sampled values such that the mean attenuation along each link matches the original transformed measurement.

OK. We apply ordinary kriging algorithm (Matheron, 1963b; Cressie, 1993b) using OrdinaryKriging function from PyKriging package (Murphy et al., 2025). We use the Exponential variogram model, with parameters inferred using PyKriging’s default L1-norm-based variogram fitting.

C.2. Diffusion posterior sampling baselines

MGDM. We implement the MGDM sampler proposed by Janati et al. (2025a) in Algorithm 2, by adapting the reference implementation⁵. In particular, the code is adapted to the VE setting. We sample the intermediate steps uniformly and use one Gibbs sampling set.

DAPS. We refer to Zhang et al. (2024, Algo 1) for the method used in the DAPS sampler implemented based on the released code⁶. We use the Langevin MCMC sampler for consistency and adapted to the VE setting.

REDDIFF. We implement the REDDIFF sampler as described in Mardani et al. (2024, Algo 1). We modify the implementation provided in released repository⁷ to the VE setting.

CREPE. We follow the algorithm presented in He et al. (2025b, Algo 1) combined with the reference code⁸ provided by the authors. We adapted the CREPE sampler to our use case of VE formulation. Following the authors, we use the prior model as a proposal and use the DPS intermediate likelihoods (also referred to as intermediate rewards) to define the annealing path that bridge the Gaussian p_T and the target π_0 .

DPS. We modify the released code⁹ that implements Chung et al. (2023, Algorithm 1) to operate within VE-setting.

⁵<https://github.com/badr-moufad/mgdm>

⁶<https://github.com/zhangbingliang2019/DAPS>

⁷<https://github.com/NVlabs/RED-diff>

⁸<https://github.com/jiajunhe98/CREPE-Controlling-diffusion-with-REPLICA-Exchange>

⁹<https://github.com/DPS2022/diffusion-posterior-sampling>

Table 6. The hyperparameters for each meteorological algorithm. The symbol “–” indicates that the corresponding hyperparameter is not applicable to the given method.

Algorithm	p	ROI	# Points per link	# Iterations	Variogram
IDW	2	6	1	–	–
GMZ	2	6	5	20	–
OK	–	–	–	–	exponential

Table 7. The hyperparameters for each posterior sampling algorithm. We use Karras scheduler with $\sigma_{\min} = 2 \times 10^{-3}$ and $\sigma_{\max} = 100$ for GP experiments and $\sigma_{\min} = 2 \times 10^{-3}$ and $\sigma_{\max} = 80$ for rain field experiments.

Algorithm	Base hyperparameters	Tasks	
		Gaussian Process	Real CML links
DAPS	$n_{\text{steps}} = 100$ $N_{\text{ode}} = 5$ Min ratio = 0.01 MCMC sampler = Langevin $\rho = 7$	MCMC steps = 100 $\eta_0 = 5 \times 10^{-4}$	MCMC steps = 50 $\eta_0 = 2 \times 10^{-4}$
DPS	$\rho = 7$	$n_{\text{steps}} = 320$ $\gamma = 4$	$n_{\text{steps}} = 420$ $\gamma = 1$
MGDM	$\rho = 7$ $\text{lr} = 3 \times 10^{-2}$ n_gibbs_repetitions = 1 n_gradient_repetitions = 10	$n_{\text{steps}} = 32$ n_denoising_steps = 3	$n_{\text{steps}} = 50$ n_denoising_steps = 5
MGPS	$\rho = 7$ $\text{lr} = 3 \times 10^{-2}$ n_gradient_steps = 10	$n_{\text{steps}} = 64$	$n_{\text{steps}} = 32$
REDDIFF	$n_{\text{steps}} = 1000$ $\rho = 5$ obs_weight = 1 gradterm_weight = 1	$\text{lr} = 10^{-1}$	$\text{lr} = 5 \times 10^{-3}$
TDS	$\rho = 7$	$n_{\text{steps}} = 320$ $\gamma = 4$ n_particles = 10	$n_{\text{steps}} = 420$ $\gamma = 1$ n_particles = 4

TDS. We implement Wu et al. (2023, Algorithm 1) in the VE setting. As a proposal distribution, we use DPS (Chung et al., 2023, Algorithm 1), which differs from the original proposal by normalizing the log-gradient of the intermediate likelihood. For the variance of the intermediate likelihoods, we use the surrogate $\sigma_i^2 + (\tau\sigma_t)^2$, where τ is a hyperparameter set to $\tau = 1$, as it yields the best empirical performance.

MGPS. We implement the MGPS (Moufad et al., 2025, Algo 1) based on the released code¹⁰ by adapting it to our VE setting. We use $\eta = 0.5$ for selecting the midpoint and we do not use warm start for the algorithm.

D. Details on Siddon Algorithm

We provide implementation details for computing the intersection-length weights Δ^i in Equation (4), i.e., the lengths of intersection between the i -th CML path and the $H \times W$ grid cells.

Grid Parametrization. Consider a regularly spaced grid with vertical and horizontal grid lines located at

$$x = x_{\text{ref}} + c \Delta x, \quad y = y_{\text{ref}} + r \Delta y, \quad c, r \in \mathbb{Z},$$

where $\Delta x, \Delta y > 0$ are the grid spacings and $(x_{\text{ref}}, y_{\text{ref}})$ specifies the grid origin. Under the affine change of variables $\tilde{x} := (x - x_{\text{ref}})/\Delta x$ and $\tilde{y} := (y - y_{\text{ref}})/\Delta y$, these grid lines map to integers defined by (\tilde{x}, \tilde{y}) . Hence, intersection computations can be carried out in the normalized coordinates and mapped back to the original coordinate system.

¹⁰<https://github.com/YazidJanati/mgps>

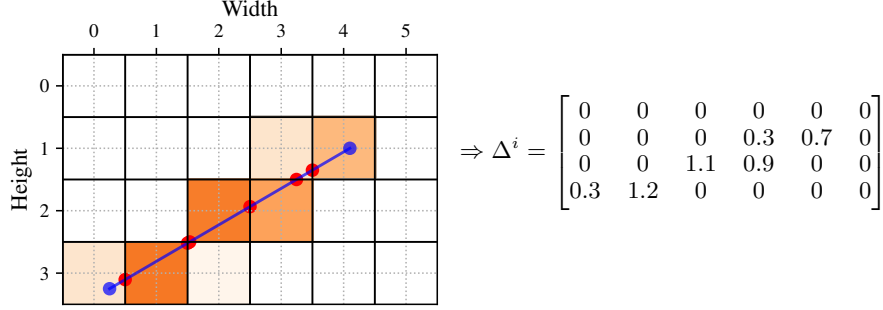


Figure 6. Illustration of a line sensor on a 6×4 grid. The blue dots define the line sensor whereas the red dots mark its intersections with the two-dimensional grid. The color intensity of each cell is proportional to the intersection length: the darker, the higher.

Considered convention. In our setting, the radar maps use the origin $(-\frac{1}{2}, -\frac{1}{2})$ and unit spacing in both directions, i.e., $\Delta x = \Delta y = 1$. Indexing cells by the integer coordinates of their centers $(c, r) \in \mathbb{Z}^2$ places the cell boundaries at $c \pm \frac{1}{2}$ and $r \pm \frac{1}{2}$; equivalently, cell centers lie at integer coordinates.

Therefore, the grid lines of the considered $H \times W$ discretization are located at

$$x = c + \frac{1}{2}, \quad y = r + \frac{1}{2}, \quad c \in \{-1, \dots, W-1\}, \text{ and } r \in \{-1, \dots, H-1\}.$$

Line Parameterization. For a given link, let $\mathbf{s}_0, \mathbf{s}_1 \in \mathbb{R}^2$ denote its start and end points, and define the affine interpolation

$$\mathbf{s}_t := \mathbf{s}_0 + t(\mathbf{s}_1 - \mathbf{s}_0), \quad t \in [0, 1].$$

We denote coordinates by $[\mathbf{s}_t]_x$ and $[\mathbf{s}_t]_y$; in particular, $[\mathbf{s}_0]_x, [\mathbf{s}_0]_y$ and $[\mathbf{s}_1]_x, [\mathbf{s}_1]_y$ for the start and end points respectively.

Algorithm. Let $\mathbf{d} := \mathbf{s}_1 - \mathbf{s}_0$ with $d_x := [\mathbf{d}]_x$ and $d_y := [\mathbf{d}]_y$. We seek parameters $t \in (0, 1)$ such that \mathbf{s}_t lies on a grid line. For each vertical grid line $x = c + \frac{1}{2}$ with $d_x \neq 0$, the corresponding parameter is

$$t_c^x := \frac{(c + \frac{1}{2}) - [\mathbf{s}_0]_x}{d_x}$$

and we retain those satisfying $t_c^x \in (0, 1)$. Analogously, for each horizontal grid line $y = r + \frac{1}{2}$ with $d_y \neq 0$,

$$t_r^y := \frac{(r + \frac{1}{2}) - [\mathbf{s}_0]_y}{d_y},$$

retaining those with $t_r^y \in (0, 1)$. We then form

$$T := \{0, 1\} \cup \{t_c^x : t_c^x \in (0, 1)\} \cup \{t_r^y : t_r^y \in (0, 1)\},$$

where the set union removes duplicates (e.g., when the line crosses a grid corner). Sorting T yields

$$0 = t_0 < t_1 < \dots < t_N = 1.$$

Consecutive parameters define sub-segments that lie within single grid cells. Their Euclidean lengths are

$$\delta_n := \|\mathbf{s}_{t_{n+1}} - \mathbf{s}_{t_n}\|_2 = \|\mathbf{s}_1 - \mathbf{s}_0\|_2 (t_{n+1} - t_n), \quad n = 0, \dots, N-1.$$

We store the weights as a sparse matrix $\Delta^i \in \mathbb{R}_{\geq 0}^{H \times W}$, where $[\Delta^i]_{r,c}$ equals the length of the portion of the link in cell (c, r) . Vectorizing Δ^i yields the coefficients $\{\Delta_k^i\}_{k=1}^{HW}$ used in Equation (4). An example of the resulting sparse weight matrix is shown in Figure 6.

E. Closed-form Expression of the Oracle Posterior

Setting. We recall that the considered setting: a linear inverse problem where the prior X is a GP $X \sim \mathcal{GP}(0, k)$ on $[-5, 5]$, with the RBF kernel

$$k(s, s') = \exp\left(-\frac{(s - s')^2}{2\ell^2}\right), \quad \ell = 0.6. \quad (10)$$

The inverse problem is defined by

$$Y_i = \int_{a_i}^{b_i} X(s) ds + \sigma Z_i, \quad Z_i \sim \mathcal{N}(0, 1), \quad (11)$$

where $\{[a_i, b_i]\}_{i=1}^m$ are the considered integration intervals and $\{Z_i\}_{i=1}^m$ are mutually independent and independent of X . Since the inverse problem involves linear transformations of the GP prior, the posterior is also a GP with closed-form mean and covariance (Rasmussen & Williams, 2006) that writes

$$\begin{aligned} \mu_{X|y}(s) &= \mathbf{k}_y(s)^\top (\mathbf{K}_{yy} + \sigma^2 \mathbf{I})^{-1} \mathbf{y}, \\ k_{X|y}(s, s') &= k(s, s') - \mathbf{k}_y(s)^\top (\mathbf{K}_{yy} + \sigma^2 \mathbf{I})^{-1} \mathbf{k}_y(s'), \end{aligned}$$

where $\mathbf{k}_y(s) \in \mathbb{R}^m$ is the covariance between $X(s)$ and the i -th observation y_i , namely $\text{cov}(X(s), y_i)$; and $\mathbf{K}_{yy} \in \mathbb{R}^{m \times m}$ covariance between the observations $[y_1, \dots, y_m]$, namely $[\mathbf{K}_{yy}]_{ij}$ is the covariance between the i -th and j -th observations $\text{cov}(y_i, y_j)$. Getting the closed-form expression of the posterior GP amounts to deriving the expressions of $[\mathbf{k}_y(s)]_i$ and $[\mathbf{K}_{yy}]_{ij}$ for all i, j in $\llbracket 1, m \rrbracket$.

Derivation of the covariances. The covariance between the i -th observation and $X(s)$ writes as

$$\begin{aligned} [\mathbf{k}_y(s)]_i &= \text{cov}\left(X(s), \int_{a_i}^{b_i} X(s') ds' + \sigma Z_i\right) \\ &= \int_{a_i}^{b_i} \text{cov}(X(s), X(s')) ds' \\ &= \int_{a_i}^{b_i} k(s, s') ds' \end{aligned}$$

where the second equality follows from the linearity of the integral and the independence between X and Z_i . The value $[\mathbf{k}_y(s)]_i$ can be numerically approximated using the Error Function erf ¹¹

$$[\mathbf{k}_y(s)]_i = \ell \sqrt{\frac{\pi}{2}} \left[\text{erf}\left(\frac{b_i - s}{\sqrt{2}\ell}\right) - \text{erf}\left(\frac{a_i - s}{\sqrt{2}\ell}\right) \right]. \quad (12)$$

Similarly, the covariance between the i -th and j -th observations writes

$$\begin{aligned} [\mathbf{K}_{yy}]_{ij} &= \text{cov}\left(\int_{a_i}^{b_i} X(s) ds + \sigma Z_i, \int_{a_j}^{b_j} X(s') ds' + \sigma Z_j\right) \\ &= \int_{a_i}^{b_i} \int_{a_j}^{b_j} \text{cov}(X(s), X(s')) ds ds' + \sigma^2 \delta_{i=j} \\ &= \int_{a_i}^{b_i} \int_{a_j}^{b_j} k(s, s') ds ds' + \sigma^2 \delta_{i=j}, \end{aligned}$$

where $\delta_{i=j}$ equals 1 if $i = j$ and zero otherwise. The first term on the right-hand side can be computed by: (i) using the result in Equation (12), and (ii) integrating by leveraging the formula of the primitive of $s \mapsto \text{erf}(s/\sqrt{2}\ell)$, namely

$$H(z) = z \cdot \text{erf}\left(\frac{z}{\sqrt{2}\ell}\right) + \sqrt{\frac{2}{\pi}} \ell \exp\left(-\frac{z^2}{2\ell^2}\right).$$

¹¹<https://docs.pytorch.org/docs/stable/generated/torch.erf.html>

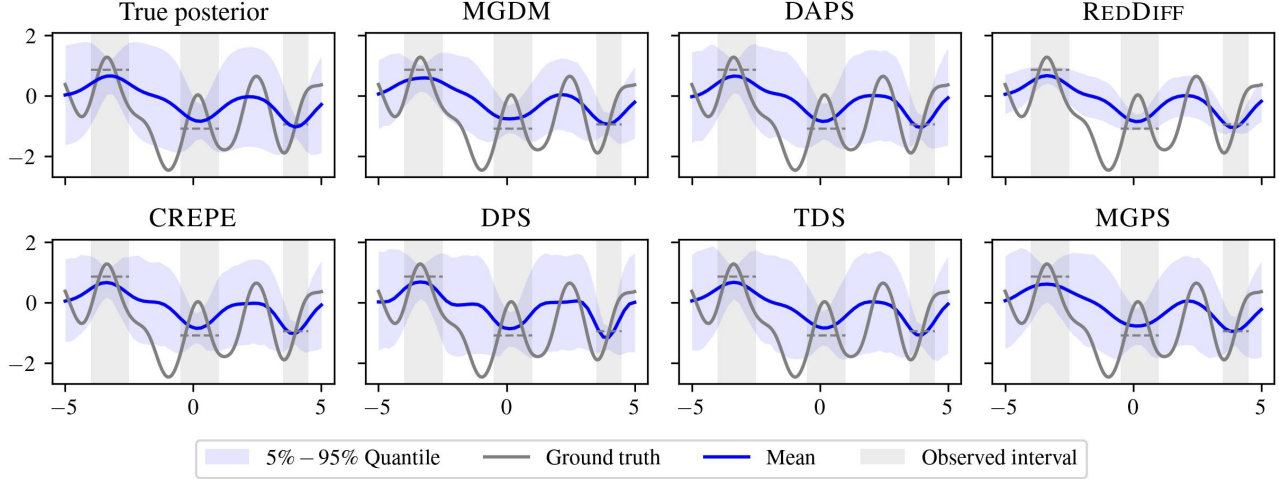


Figure 7. Extended results of Figure 3. Comparison between the reconstructions of the baselines on the inverse problem with diffusion prior on the setting of GP. The y-axis shows intensities while the x-axis represents a one-dimensional grid of the $[-5, 5]$ interval. The dashed horizontal lines depict values of the integral over the observed intervals.

Putting it together, the expression of $[\mathbf{K}_{yy}]_{ij}$ writes as

$$[\mathbf{K}_{yy}]_{ij} = \ell \sqrt{\frac{\pi}{2}} \left[H(b_i - a_j) - H(a_i - a_j) - H(b_i - b_j) + H(a_i - b_j) \right] + \sigma^2 \delta_{i=j}.$$

F. Censored Gaussian Process

Setting revisited. We revisit the setting in Section 3.1. We assume that the rain field $X : \Omega \subset \mathbb{R}^2 \rightarrow \mathbb{R}_+$ is described by a left-censored GP with a power transformation $\beta > 1$

$$X(\mathbf{s}) = \max\left(0, V(\mathbf{s})^\beta\right), \quad \mathbf{s} \in \Omega \subset \mathbb{R}^2,$$

namely, $V \sim \mathcal{GP}(\mu, k)$ being a stationary GP with constant $\mu \in \mathbb{R}$ and kernel

$$k(\mathbf{s}, \mathbf{s}') = \sigma^2 \exp\left(-\frac{1}{2}(\mathbf{s} - \mathbf{s}')^\top \mathbf{Q}^{-2} (\mathbf{s} - \mathbf{s}')\right), \quad \sigma > 0, \quad \mathbf{Q} = \text{Diag}(\ell_1, \ell_2) \in \mathbb{R}^{2 \times 2},$$

where the positive definite matrix \mathbf{Q} is meant to account for anisotropy of the field. The domain of interest $\Omega \subset \mathbb{R}^2$ is discretized in a grid of $H \times W$ at the points $\{s_k\}_{k=1}^{HW}$ and we assume to have access to the realization of N of the discretized field $x_i \in \mathbb{R}_+^{HW}$, that is, for $i \in \llbracket 1, N \rrbracket$, we have

$$x_i = \max(0, v_i^\beta), \quad \text{where} \quad v_i \sim \mathcal{N}(\mu \mathbf{1}, \Gamma(\mathbf{Q})) \quad \text{and} \quad \Gamma_{\ell, j} = k(\mathbf{s}_\ell, \mathbf{s}_j), \quad \text{for } 0 \leq \ell, j \leq HW$$

The goal is to estimate the parameters of the latent model $(\mu, \mathbf{Q}, \sigma, \beta)$. To do so, we use the EM algorithm and proceed first by deriving the algorithm when $\beta = 1$, and then generalize to $\beta > 1$.

Parameters estimation of the model. One way to estimate the parameters and avoid optimizing jointly β , is to fit the model parameters for different values of β and then select the configuration that gives the best classifier two-sample test.

F.1. EM algorithm for $\beta = 1$

The joint model factorizes as

$$p(x_i, v_i) = \delta_{\max(0, v_i)}(x_i) p_V(v_i),$$

where p_V denotes the marginal distribution of v_i and is given by the Gaussian $\mathcal{N}(\mu\mathbf{1}, \Gamma(\mathbf{Q}))$. For a given observation x_i , we define the index sets corresponding to positive and zero components as

$$I_i^+ = \{k : [x_i]_k > 0\}, \quad I_i^0 = \{k : [x_i]_k = 0\},$$

and denote by (x_i^+, x_i^0) the restriction of x_i to I_i^+ and I_i^0 , respectively.

E-step. The E-step consists in sampling from the posterior $p_{V|X}(\cdot | x_i)$, which factorizes as

$$p_{V|X}(v_i | x_i) \propto \delta_{x_i^+}(v_i^+) \times \mathbf{1}_{\{v_i^0 \leq 0\}} p_V(v_i^0 | v_i^+ = x_i^+). \quad (13)$$

The second factor corresponds to a truncated multivariate Gaussian distribution. Samples are obtained via Gibbs sampling, leveraging the fact that one-dimensional truncated Gaussian conditionals can be sampled exactly using inverse transform sampling.

M-step. At iteration k , posterior samples $v_i \sim p_{V|X}^{(k)}(\cdot | x_i)$ are drawn using the current parameter estimates. The parameters (μ, Q) are then updated by maximizing the complete-data log-likelihood,

$$\arg \max_{\mu, \mathbf{Q}, \sigma} \sum_{i=1}^N \log p_V(v_i),$$

which corresponds to standard maximum likelihood estimation for a multivariate Gaussian model.

F.2. EM algorithm for $\beta > 1$

For $\beta > 1$, the posterior distribution $p_{V|X}^\beta(\cdot | x_i)$ no longer involves a truncated multivariate Gaussian. Nevertheless, its density admits a closed-form expression:

$$p_{V|X}^\beta(v_i^0 | v_i^+ = x_i^+) = p_V\left((v_i^0)^{1/\beta} | v_i^+ = x_i^+\right) \left| \det\left(\mathbf{J}_f(v_i^0)\right) \right|, \quad (14)$$

where $\mathbf{J}_f(v_i^0)$ denotes the Jacobian of the elementwise power transformation $f(v) = v^\beta$. The Jacobian is diagonal and can be computed exactly and efficiently.

E-step. The E-step is performed using a Metropolis-within-Gibbs scheme. We use the same procedure in E-step of the case $\beta = 1$ as a proposal distribution, and acceptance ratios are computed using the density in (14).

M-step. Although the power transformation modifies the posterior density, it does not affect the model parameters. Consequently, the M-step mirrors that of the $\beta = 1$ case, with the exception that posterior samples are transformed back by applying the inverse power. Specifically, parameter updates are obtained by maximizing

$$\arg \max_{\mu, \mathbf{Q}, \sigma} \sum_{i=1}^N \log p_V\left(v_i^{1/\beta}\right).$$

which, similarly, correspond maximum likelihood estimation for a multivariate Gaussian model expect the inputs are $v_i^{1/\beta}$.

F.3. Practical Computational Challenges

While the procedure described above enables learning from censored processes, it scales poorly in our current high-dimensional setting, where rain fields have dimension $48 \times 36 = 1728$ and nearly 50% of the entries are censored. The E-step requires posterior sampling to impute the censored coordinates of each rain field by sampling from a truncated multivariate Gaussian distribution. Since the censored coordinates vary across rain fields, this limits the ability to leverage vectorized computation and makes estimation prohibitively dependent on the number of rain fields, which is 21,196 in our setting. In addition, using Gibbs sampling for the truncated multivariate Gaussian requires a long burn-in period due to the dimensionality of the data.

G. Examples of Reconstructions in CML Experiments

We present qualitative examples of rain field reconstructions from CML measurements on the OpenMRG dataset. The comparison includes all considered baselines, both meteorological and diffusion-based methods. Three representative reconstruction examples are shown.

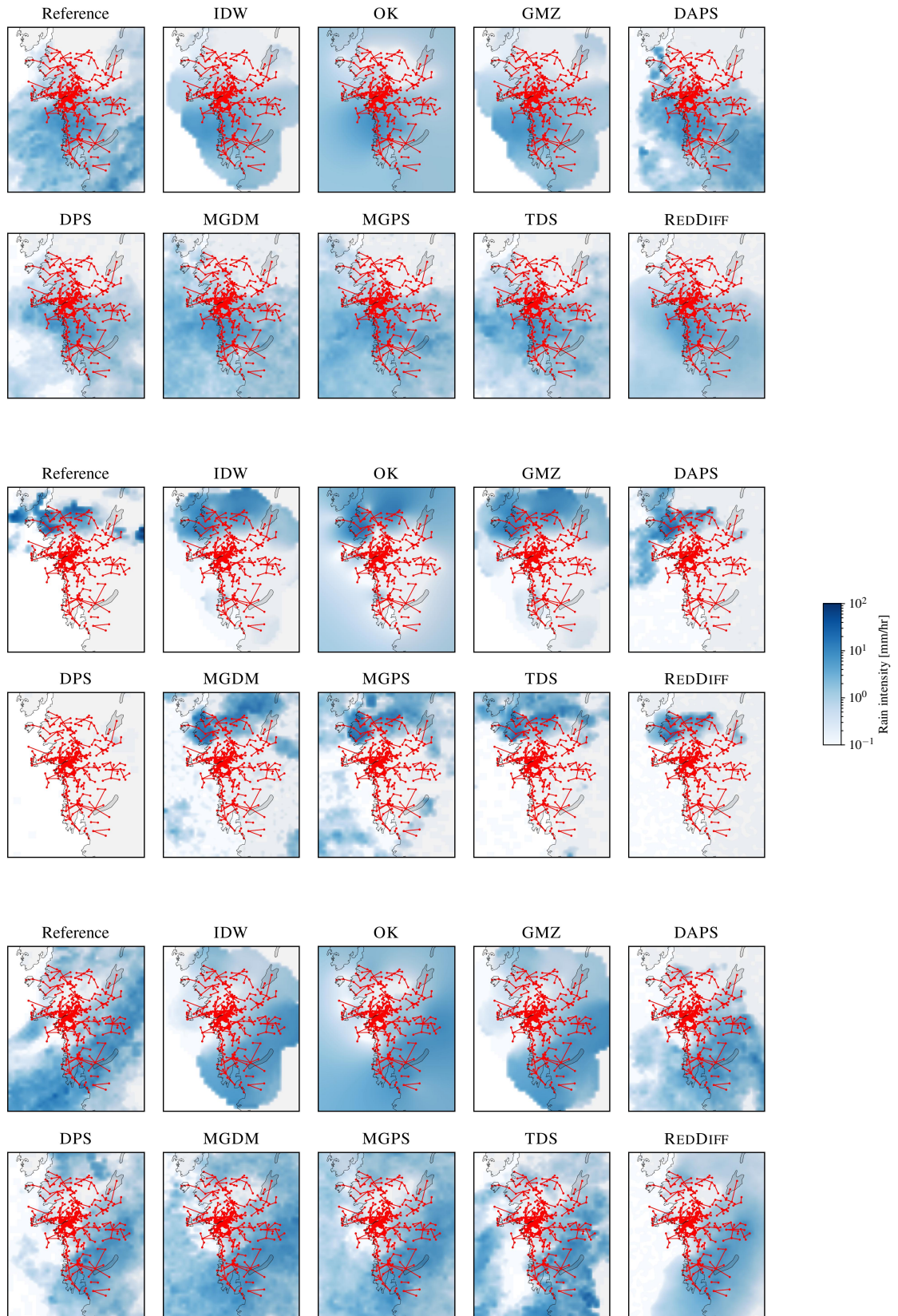


Figure 8. Qualitative comparisons of rain field reconstructions on real CMLs links from OpenMRG dataset on three reconstruction tasks. The network of CMLs is depicted in red.

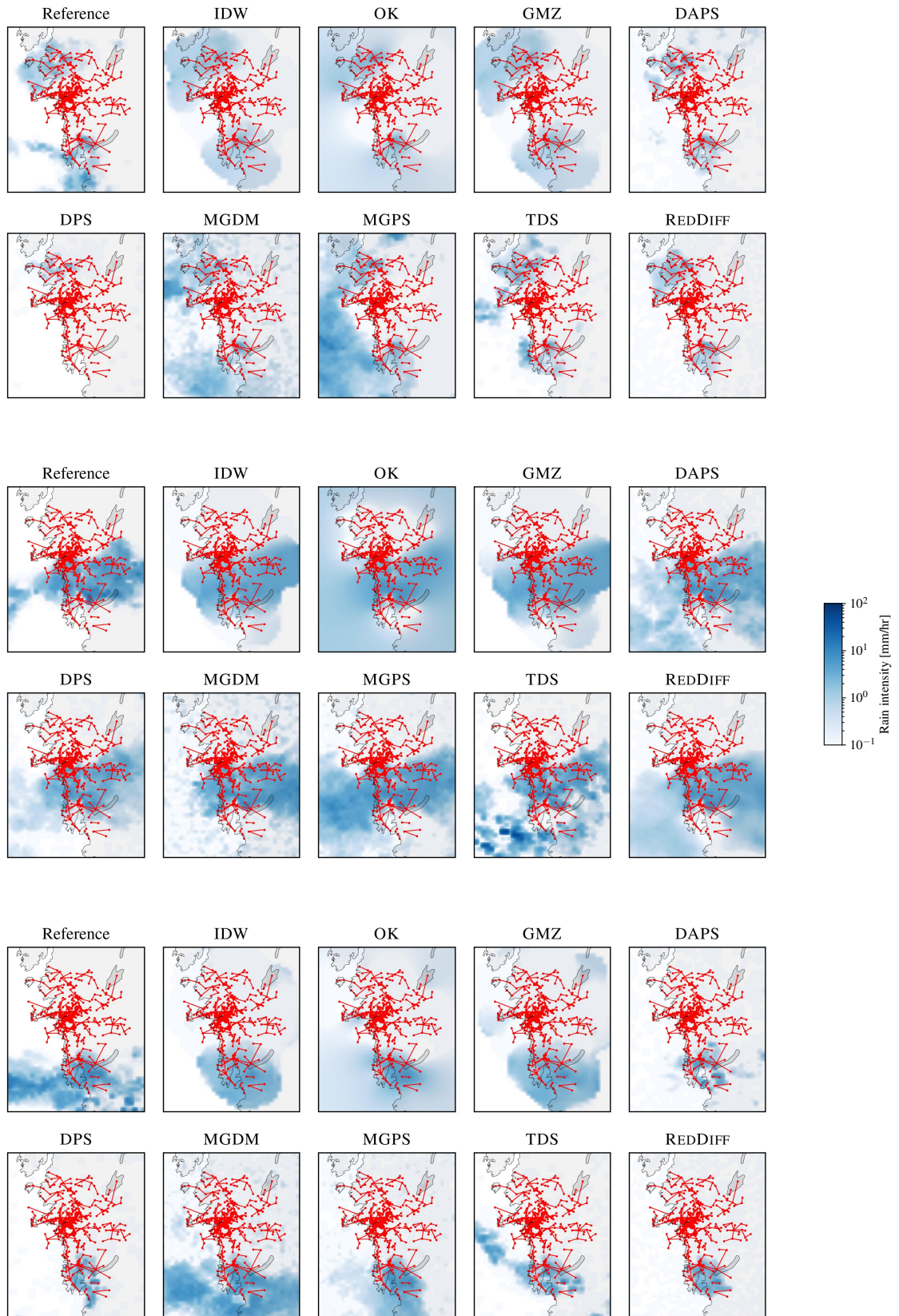


Figure 9. Another set of qualitative comparisons of rain field reconstructions on real CMLs links from OpenMRG dataset on three reconstruction tasks. The network of CMLs is depicted in red.